Master Thesis

Dynamics of ultrasound-driven coated microbubbles confined in viscoelastic capillaries

Author:
Fleur Vialle

Examination committee
Assis.prof.dr. G.P.R. Lajoinie (daily supervisor)
Prof.dr. M. Versluis (chair committee)
Prof.dr.ir. N. Bosschaart (external member)
Prof. E. Hachem (external member)

February 9, 2024

Physics of Fluids
Faculty of Science and Technology
University of Twente

Physics of Fluids

UNIVERSITY OF TWENTE.

Abstract

Phospholipid coated microbubbles are widely used as ultrasound contrast agents for both diagnostic and therapeutic applications. The dynamics of ultrasound-driven coated microbubbles have been primarily investigated in unbounded fluids. However, when microbubbles are in the bloodstream, they are often confined in viscoelastic capillaries. Numerical and few experimental studies have shown that the viscoelastic confinement affects the resonance response of microbubbles. To increase the sensitivity of diagnostic and therapeutic ultrasound in small vessels, we need to model the relation between bubble response and vessel properties, such as stiffness and diameter. In this work, we have taken the initial steps towards this model by performing experimental research, studying methods for signal filtering and developing a 2D numerical simulation. We have built an experimental setup combining ultrasound imaging and optical high speed imaging. The acoustic response from nonlinear microbubbles and linear hollow glass beads inside a capillary phantom has been measured using chirp and narrowband pulses. Using Pulse Inversion (PI) the fundamental and harmonic responses have been successfully isolated. We have demonstrated that SVD filtering allows for a quantitative analysis of the frequency response. However, the relation between the obtained amplitudes after SVD filtering and the acoustic response from microbubbles and beads is yet to be investigated. Both the beads and bubbles showed higher harmonics implying that the measurements currently lack the sensitivity to distinguish the nonlinear microbubble response from nonlinear propagation effects. The numerical simulation of a microbubble between elastic walls showed microbubble oscillations and wall displacement driven by the ultrasound. The oscillation amplitude of the microbubble showed a resonance behaviour, where a decrease in resonance frequency was observed with increasing ultrasound pressure consistent with literature. No dependence of resonance frequency on wall stiffness was observed because the microbubble was not sufficiently confined by the walls. In future research, the effects of nonlinear propagation should be quantified and reduced, the use of SVD filtering and other filtering methods needs to be further studied and the numerical simulation should be transitioned to 3D.

Contents

1 Introduction

Ultrasound imaging is one of the most widely used medical imaging techniques, together with Magnetic Resonance Imaging (MRI) and X-ray computed tomography (CT), because of its cost effectiveness and safety. Ultrasound imaging involves no harmful radiation unlike CT. Moreover, in contrast to MRI and CT scanners, ultrasound machines are small portable devices. [1, 2] One of the most common and well-known applications of ultrasound imaging is in obstetrics, where it is used for fetal scanning of pregnant women. Here, the fetal tissue scatters the ultrasound waves much more than the hypoechoic amniotic fluid causing the fetus to appear bright in the ultrasound image against a darker background. Next to fetal scanning, there exist many more applications of medical ultrasound in both diagnostics and therapeutics. In oncology, for example, ultrasound can be used to detect lesions and for targeted drug delivery. In cardiology, myocardial perfusion is assessed using ultrasound as well as left ventricular function. Moreover, ultrasound is used for imaging blood flow characteristics in the vasculature to detect, for instance, plaques or assess vascular stenosis. [3–5] Blood, however, is a poor ultrasound scatterer and therefore generates little contrast in ultrasound imaging, which is problematic for flow imaging. [6]

Ultrasound contrast agents (UCAs), which are injected intravenously, enhance the visibility of blood. These contrast agents are microbubbles of about $1\text{-}10\,\mu\mathrm{m}$ in diameter. They are usually filled with high-molecular-weight gasses, typically perfluorobutane (C_4F_{10}) or sulfur hexafluoride (SF_6), and coated by a phospholipid shell. They enhance image contrast in two ways. First, the large difference between the acoustic impedance of the gas inside the microbubble and the surrounding fluid leads to the scattering of ultrasound. Second, due to the large compressibility of the gas, the oscillatory driving pressure of the ultrasound field results in microbubble expansion and contraction. This bubble response can be compared to a mass-spring system, where the gas represents the spring and the surrounding fluid represents the mass pushing on the surface of the microbubble. Similar to a mass-spring system, the microbubble shows resonance behaviour. Therefore, the effective scatter cross section is increased up to several orders of magnitude with respect to a rigid sphere with the same acoustic impedance and the same size. Moreover, when driven at resonance, the microbubbles behave non-linearly leading to the emission of higher harmonics and subharmonics. [6, 7] These higher harmonics can be used to detect the acoustic response from microbubbles while suppressing the response from linear tissue.

Experimental studies have shown that the resonance behaviour depends on microbubble size, acoustic driving pressure and shell characteristics. It was indeed shown by Van der Meer et al [8] that larger microbubbles resonate at lower frequencies than smaller microbubbles. The resonance frequency of a coated bubble is found to be increased compared to that of an uncoated bubble due to the stiffness of the shell [6]. Segers et al. [9] have shown that increasing the acoustic driving pressure reduces the resonance frequency. The resonance of microbubbles in unbounded fluids is well-described by Rayleigh-Plesset-type equations and the nonlinear effect of the shell can be described by the Marmottant model [6]. However, when microbubbles are located in viscoelastic capillaries, which have a diameter down to 10 µm [10], the assumption of an unbounded fluid no longer holds. Numerical studies have been performed on the effect of soft viscoelastic confinement on the resonance of microbubbles at low diagnostic pressures. These studies showed that confinement of bubbles in rigid vessels decreases the natural frequency, while the frequency increases in the case of compliant vessels. Besides vessel stiffness, the resonance frequency is also predicted to depend on vessel size [10–13].

Linear and nonlinear bubble scattering thus depends on vessel properties. Understanding the relationship between bubble response and vessel properties can increase the sensitivity of diagnostic and therapeutic ultrasound in small vessels. Moreover, if the bubble response is linked to vessel properties, it could potentially be used for characterising vessels and might eventually even be used for differentiating between diseased capillaries, in for example tumors, and healthy capillaries since these are mechanically different [14, 15]. To this end, however, it is necessary to model the relation between bubble response and vessel properties, such as stiffness and diameter.

Few experimental studies have been performed on microbubbles confined in capillary tubes, and these were mainly based on optical high speed imaging [16–18]. Moreover, existing experimental studies typically use rigid capillaries, and/or high pressures for therapeutic applications. The numerical studies conducted so far still require experimental validation and do not take into account the effect of the bubble shell on the resonance behaviour. In other words, the nonlinear response of phospholipid-coated microbubbles confined in viscoelastic capillaries is still largely unknown.

The aim of this research is to provide a model, using a combination of numerical simulations and experiments, to relate the microbubble response to vessel properties, i.e. stiffness and diameter. The numerical simulations will be validated using the experimental results, after which the numerical simulations can be used to explore a multitude of variables in a controlled environment. This thesis laid the foundation for this research by performing experimental research, signal filtering and numerical simulations. For the experimental research, we built a setup combining ultrasound and optical imaging. We used monodisperse bubbles, which have a narrow resonance frequency distribution owing to their uniform size. This enhances the ability to observe shifts in resonance frequency caused by vessel properties. Moreover, the consistent resonance frequency of these bubbles improves the signal-to-noise ratio (SNR) compared to using polydisperse microbubbles. We investigated different types of ultrasound waveforms to explore their effectiveness in detecting the microbubble response. Moreover, we studied the use of pulse inversion to separate the microbubble response from tissue background. After data acquisition, we investigated the use of singular value decomposition (SVD) filtering in the data analysis for distinguishing the response of the moving microbubbles and beads from the static tissue response. Complementary to the experimental study, we developed a first version of a finite element simulation to numerically study the dynamics of ultrasound-driven coated microbubbles confined between elastic walls.

2 | Background

2.1 Bubble dynamics

The dynamics of a spherical coated bubble surrounded by an infinite, incompressible and Newtonian fluid and driven by an external ultrasound field are governed by the Rayleigh-Plesset equation [6, 9]:

$$\begin{aligned}\rho_l\left(R\frac{\mathrm{d}^2R}{\mathrm{d}t^2}+\frac{3}{2}\frac{\mathrm{d}R}{\mathrm{d}t}^2\right) = &\left(P_0+\frac{2\sigma\left(R_0\right)}{R_0}\right)\left(\frac{R_0}{R}\right)^{3\kappa}\left(1-\frac{3\kappa\frac{\mathrm{d}R}{\mathrm{d}t}}{c_l}\right)\\ &-\frac{2\sigma}{R}-\frac{4\mu_l\frac{\mathrm{d}R}{\mathrm{d}t}}{R}-P_0-P_\mathrm{A}(t)-\frac{4\kappa_\mathrm{s}\frac{\mathrm{d}R}{\mathrm{d}t}}{R^2}.\end{aligned} \tag{2.1}$$

In this equation, the time-dependent radius of the bubble is represented by R and the initial bubble radius is given by R_0. $\frac{\mathrm{d}R}{\mathrm{d}t}$ and $\frac{\mathrm{d}^2R}{\mathrm{d}t^2}$ are the bubble wall velocity and acceleration, respectively. P_0 and $P_\mathrm{A}(t)$ represent the atmospheric pressure and the acoustic driving pressure,respectively. The liquid properties are included by the liquid viscosity μ_l, the density ρ_l and the speed of sound in the liquid c_l. Moreover, κ represents the polytropic exponent.

The effect of the phospholipid shell on the bubble dynamics is included in the surface tension σ and in the final pressure term, i.e. $\frac{4\kappa_s}{R^2}\frac{\mathrm{d}R}{\mathrm{d}t}$. This pressure term takes into account the viscous energy dissipation in the microbubble shell, with κ_s being the shell viscosity, while the surface tension accounts for the shell elasticity χ.

The presence of the shell results in non-linear behaviour of the bubble. Upon compression, the shell starts to buckle, while shell rupture occurs upon large expansion of the bubble. This non-linear bubble dynamics are accounted for by the radial dependency of the surface tension, which is described by the Marmottant model (Figure 2.1) [19]. The Marmottant model states that the surface tension reduces to zero below a certain radius due to buckling of the shell. When the bubble expands too much, the radius will rupture leading to a surface tension equal to the surface tension of the surrounding fluid. In between the rupture and buckling radius, the surface tension increases with increasing bubble radius. According to the Marmottant model, the surface tension is thus given by:

$$\sigma(R) = \begin{cases} 0 & \text{if} \quad R \le R_\mathrm{b} \\ \chi\left(\frac{R^2}{R_\mathrm{b}^2}-1\right) & \text{if} \quad R_\mathrm{b} \le R \le R_\mathrm{r} \\ \sigma_\mathrm{water} & \text{if} \quad R \ge R_\mathrm{r}. \end{cases} \tag{2.2}$$

with R_b and R_r the buckling and rupture radius, respectively. [6, 19]

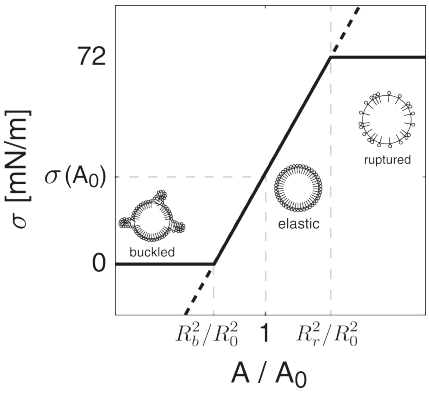

Figure 2.1: Surface tension as a function of the bubble radius as described by the Marmottant model. Buckling or rupture of the shell occurs upon compression or expansion, respectively. In the intermediate regime the shell behaves elastically. Figure is adapted from [6].

2.2 Harmonic imaging

The harmonic signal generated by the nonlinear microbubbles can be separated from the fundamental signal using a method called Pulse Inversion (PI). Figure 2.2 shows the principle of the pulse inversion technique.

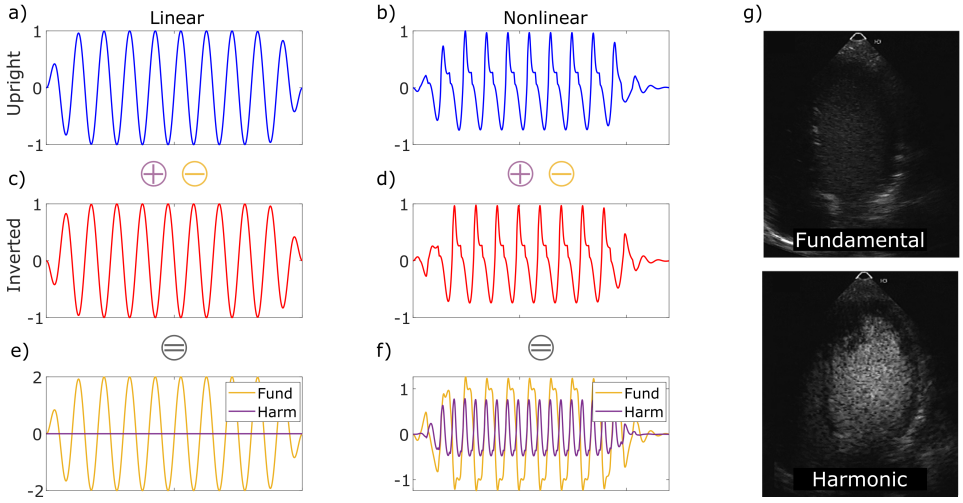

Figure 2.2: (a-b) Response of a linear and nonlinear scatterer to the upright pulse. (c-d) Response of a linear and nonlinear scatterer to the inverted pulse. (e) Fundamental and harmonic signal obtained after respectively subtracting or adding the response of a linear scatterer to the upright and inverted pulse. (f) Fundamental and harmonic signal obtained after respectively subtracting or adding the response of a nonlinear scatterer to the upright and inverted pulse. (g) Fundamental and harmonic image of the left ventricle filled with contrast agent, obtained from [20].

In PI, two waveforms are successively transmitted with a suitable delay time in between. The second pulse is the inverted version of the first pulse. For linear scatterers, the echo from the second pulse (Figure 2.2c) will be the inverse of the echo from the first pulse (Figure 2.2a). In the case of nonlinear scatterers like microbubbles, however, the echo from the second pulse (Figure 2.2d) will not be the

exact inverse of the echo from the first pulse (Figure 2.2b). Instead, the nonlinear response to the upright and inverted pulse will be in phase after scattering. Therefore, by adding the response from the upright and the inverted pulse, the linear response cancels while the nonlinear response remains, as can be seen by comparing the purple curves in Figure 2.2e and f. In the frequency domain this implies that even harmonics are emphasized, while odd harmonics, including the fundamental, are cancelled. [21, 22] On the other hand, subtracting the response corresponding to the second pulse from the first pulse, enhances the linear fundamental response with respect to the higher harmonics. The operations to emphasize either the fundamental (RF_{fund}) or harmonic response (RF_{harm}) are summarized in the equations below:

$$RF_{\text{fund}} = \frac{e_+ - e_-}{2}, \tag{2.3}$$

$$RF_{\text{harm}} = \frac{e_+ + e_-}{2}, \tag{2.4}$$

where e_+ and e_- represent the echo from the upright and the inverted pulse, respectively. The effect of using either fundamental or harmonic ultrasound imaging on the ultrasound image can be seen in Figure 2.2g, which shows a fundamental (top) and harmonic (bottom) image of contrast agent in the left ventricle. The signal-to-tissue ratio is much better in the harmonic image than in the fundamental image.

2.3 SVD filtering

To distinguish moving microbubbles from static tissue in ultrasound data, a tool called Singular Value Decomposition (SVD) can be used. Figure 2.3 shows a schematic of the process of singular value decomposition and subsequent filtering.

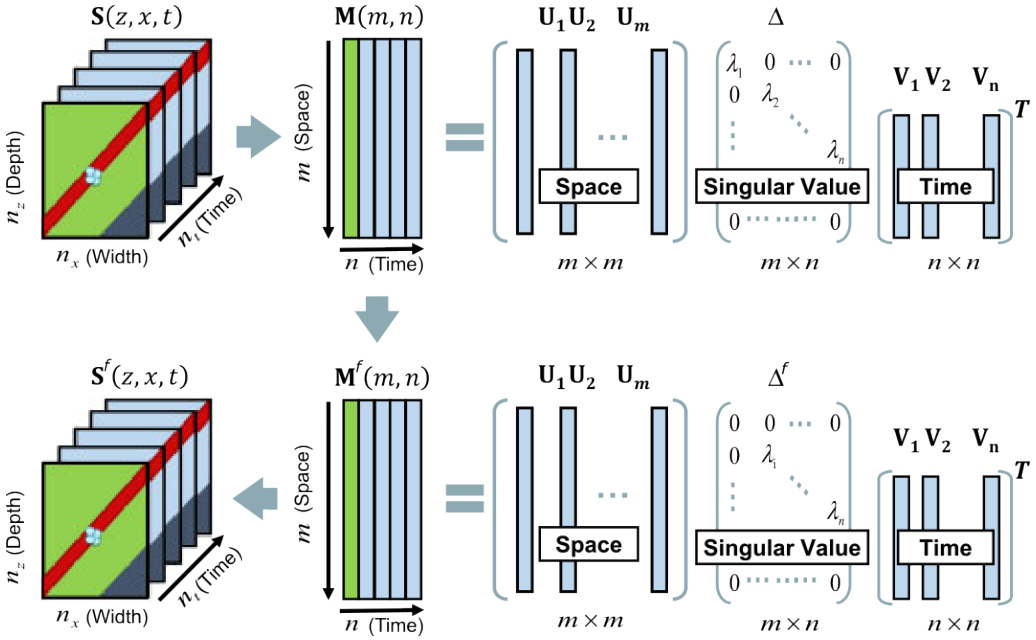

Figure 2.3: Schematic of spatio-temporal rearrangement, singular value decomposition and filtering. Adapted from [23].

The acquired ultrasound data is a three-dimensional data set $\boldsymbol{S}(z,x,t)$ with dimensions (n_z, n_x, n_t), where n_z corresponds to the number of samples in the propagation direction of the ultrasound waves, n_x equals the number of transducer elements and n_t represents the number of frames. To perform SVD, this three-dimensional data is rearranged into a two-dimensional space-time matrix $\boldsymbol{M}(m,n)$ where the number of rows m is equal to $n_z \times n_x$ and the number of columns n is equal to n_t. The SVD of this matrix $\boldsymbol{M}(m,n)$ is written as: [23–25]

$$\boldsymbol{M}(m,n) = \boldsymbol{U} \cdot \boldsymbol{\Delta} \cdot \boldsymbol{V}^*. \tag{2.5}$$

Here, $\boldsymbol{U}$ and $\boldsymbol{V}$ are unitary matrices with dimensions (m,m) and (n,n), respectively, and * is the conjugate transpose . $\boldsymbol{U}$ contains the spatial singular vectors, while $\boldsymbol{V}$ contains the temporal singular vectors. [23] The diagonal matrix $\boldsymbol{\Delta}$ has dimension (m,n) and contains the singular values λ_i. These singular values are sorted in descending order. The higher singular values and singular vectors correspond to tissue since tissue shows a high spatio-temporal coherence. The moving microbubbles are described by lower singular values and vectors due to their lower spatio-temporal coherence.

SVD filtering is performed by removing the singular values corresponding to unwanted signal. In this case, the signal from the moving microbubbles is the desired signal. To remove higher spatial coherent tissue signal, the higher singular values are set to zero in the diagonal matrix $\boldsymbol{\Delta}$. The filtered signal $\boldsymbol{M^f}$ can thus be calculated with [24]:

$$\boldsymbol{M}^f = \boldsymbol{U} \cdot \boldsymbol{\Delta}^f \cdot \boldsymbol{V}^*. \tag{2.6}$$

where $\boldsymbol{\Delta}^f$ is the truncated diagonal matrix. After the SVD filtering, the two-dimensional matrix $\boldsymbol{M}^f$ is rearranged back to the dimensions of the original three-dimensional data set resulting in $\boldsymbol{S}^f$. In this thesis, SVD filtering was performed on the RF lines received by each of the transducer elements separately.

2.4 Delay-and-sum image reconstruction curved array

The radio frequency (RF) signals received by the ultrasound transducer can be reconstructed into an image using Delay-And-Sum (DAS) beamforming. In this method, the round-trip traveltime of the wavefront from the transducer towards a scatterer and back is estimated. [26] In this research, a convex array was used for retrieving the ultrasound data. Ultrasound waves were emitted with zero time-delay between the transducer elements leading to the transmission of slightly diverging waves due to the convex shape of the transducer. Figure 2.4 shows a schematic of the delay-and-sum method.

The coordinate system is defined with the x-axis being the horizontal axis and the z-axis in the direction of wave propagation. The origin O of the system is set at the location of the virtual point source of the transmitted waves. The vertical distance between this origin and the center element of the transducer is equal to the radius of curvature R_c of the curved array.

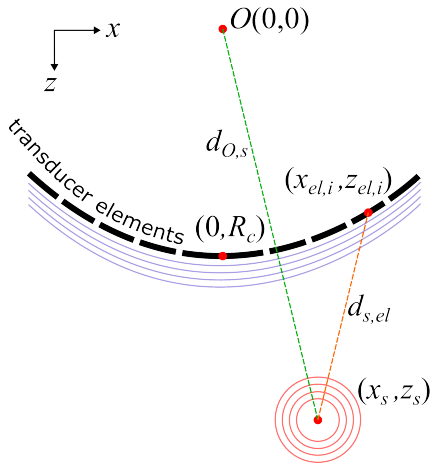

Figure 2.4: Schematic of a convex transducer transmitting ultrasound waves with zero time-delay. The origin of the waves is depicted by O. The ultrasound waves are scattered by a scatterer at position (x_s,z_s) and received by a transducer element at $(x_{el,i},z_{el,i})$. $d_{O,s}$ and $d_{s,el}$ represent the travel distance from origin to scatterer and from scatterer to transducer element i, respectively.

The travel distance for a wavefront from the origin to a scatterer with coordinates (x_s,z_s) is given by:

$$d_{O,s} = \sqrt{(z_s + R_c)^2 + x_s^2}. \tag{2.7}$$

The distance traveled by the scattered wavefront back to transducer element i is given by:

$$d_{s,el} = \sqrt{\left(z_{el,i} - z_s\right)^2 + \left(x_{el,i} - x_s\right)^2}, \tag{2.8}$$

where $x_{el,i}$ and $z_{el,i}$ represent the x- and z-coordinate of the center of the i^{th} transducer element. Combining these travel distances, the two-way traveltime of the waveform can be calculated using the following equation:

$$t_{O,el} = dt_{corr} + \frac{d_{O,s} + d_{s,el}}{c}, \tag{2.9}$$

where c is the speed of sound in the medium and dt_{corr} is a time correction given by:

$$dt_{corr} = dt_{lens} + dt_{peak}. \tag{2.10}$$

Here, dt_{lens} corrects for the different travel time through the acoustics lens of the transducer due to a different speed of sound. dt_{peak} is the time between the start of the transmitted waveform and the peak of the waveform. Since most of the scattering occurs when the peak of the transmit waveform reaches the scatterer, adding this time-to-peak to the total delay time will improve the accuracy of the image reconstruction. [27]

2.5 Tissue-mimicking materials

For the capillary phantom, a tissue-mimicking material with acoustic properties similar to those of water and typical soft tissues is needed. Moreover, to enable optical imaging of scatterers inside the phantom, optical transparency is required. Important acoustic properties are the attenuation coefficient, speed of sound and acoustic impedance. Attenuation is the phenomenon that the amplitude

of ultrasound waves decreases during propagation through a material, where a higher attenuation coefficient is associated with more attenuation. Acoustic impedance is given by $Z = \rho \cdot c$, where ρ is the material density and c the speed of sound. The proportions of reflected and transmitted ultrasound waves at interfaces depends on the difference in acoustic impedance of the two mediums. Materials having an acoustic impedance substantially different from that of water will thus strongly reflect ultrasound waves. [28, 29]

We experimented with several tissue-mimicking materials for the small vessel phantom. The first material studied was a polyacrylamide (PAA) hydrogel. As shown by A.F. Prokop et al. [30], the acoustic attenuation of PAA is low and the speed of sound and acoustic impedance of PAA are similar to water due to its high water content. Furthermore, PAA is an optically transparent material and the stiffness of the hydrogel can be easily varied by changing the concentration ratio between acrylamide monomer and the crosslinker bisacrylamide. Due to its optical transparency and acoustic properties similar to those of soft tissues, PAA hydrogel qualified as a good tissue-mimicking material for the vessel phantoms. However, hydrogel also has its drawbacks. First, one of the main constituents of PAA is the acrylamide monomer, which is a neurotoxin. Once cured, the polyacrylamide is nontoxic. Remainders of the monomer, however, can still be present. This toxicity makes the material more difficult to work with. [30] Furthermore, the hydrogel is not stable over time. When stored in air, the hydrogel dehydrates resulting in shrinking of the material, while storage in water causes the polyacrylamide to absorb the water leading to swelling of the gel. Finally, the most important drawback, when considering the production of small vessel phantoms, is the fragility of the hydrogel. [31] The pressure needed to create a flow through the small capillaries is too high causing the surrounding hydrogel to break. Therefore, this material was found not to be suitable for the small vessel phantoms.

Next, we investigated Polydimethylsiloxane (PDMS) as a possible tissue-mimicking material. Due to its higher mechanical resistance, perfusion of the small capillaries was not a problem. Moreover, it is optically transparent, relatively stable over time, easily producible and the stiffness can easily be varied by altering the base-curing agent mixing ratio [32]. The attenuation of ultrasound in PDMS, however, is much larger than the attenuation in hydrogel ($>9.8\,\mathrm{dB/cm}$ at $3\,\mathrm{MHz}$ in PDMS versus 0.21 to $0.41\,\mathrm{dB/cm}$ at $3\,\mathrm{MHz}$ in PAA [30, 33]). Moreover, the speed of sound in PDMS is much lower than in water (between 1028 and $1119\,\mathrm{m/s}$ versus $1480\,\mathrm{m/s}$ [32, 33]), while the density is similar ($1030.5\,\mathrm{kg/m^3}$ versus $997\,\mathrm{kg/m^3}$ [32]), leading to a large difference between the acoustic impedance of water and PDMS. Therefore, a significant part of the ultrasound is reflected when travelling from water into the PDMS phantom or backwards making ultrasound signal originating from the bubbles in the capillary hard to measure.

A material combining the favorable properties of PDMS and PAA is polyvinyl chloride plastisol (PVCP). PVCP is a commercially available plastic. [34] It is a white liquid substance. Upon heating the white colour disappears and the liquid becomes transparent. Once the PVCP cools down, it solidifies and turns into a transparent viscoelastic gel. It is a more resilient material than PAA hydrogel, which enables perfusion of the capillaries. Moreover, it has an acoustic impedance similar to the impedance of water and a low acoustic attenuation of 0.50 up to $0.69\,\mathrm{dB/cm}$ at $1\,\mathrm{MHz}$ depending on the hardness of the material [31, 35]. Other advantages are that the material is non-toxic, insoluble in water and stable over time [31]. Finally, multiple stiffnesses of PVCP are available and the stiffness can further be tuned using commercially available hardeners and softeners [34]. A drawback is that the PVCP becomes opaque after prolonged contact with water.

2.6 Simulation framework

To numerically study the dynamics of an ultrasound-driven microbubble confined between elastic walls, we developed a numerical simulation based on the finite element simulation library CIMLib, developed at the research institute CEMEF of MINES ParisTech. This library enables the simulation of complex fluid dynamics in geometries involving both fluid and solid domains. It can model the dynamic interaction between complex fluid flows and deformable structures. For example, it is employed to simulate the interaction between the blood flow dynamics and the arterial wall in intracranial aneurysms [36].

In the following, the mathematical framework of the simulations is first discussed. Next, the methods for solving the fluid and solid dynamics are described. Thereafter, the variational multiscale (VMS) method, which is used for stabilization, is introduced. Lastly, the methods for moving the mesh and coupling the solid and the fluid domain are explained.

2.6.1 Arbitrary Lagrangian-Eulerian framework

Two descriptions of motion are used in continuum mechanics: the Eulerian and Lagrangian description. When the movement of particles in the flow field is followed, it is called the Lagrangian description. In the Eulerian description, motion is observed at specific fixed locations. [37, 38] When a Lagrangian algorithm is used in numerics, the individual nodes of the grid move along with the particles. This yields an accurate description of, for example, moving interfaces. However, the use of Lagrangian algorithms for modelling flow is not optimal because of large deformations resulting in frequent remeshing. For fluid flow, Eulerian algorithms are widely used. In Eulerian algorithms the continuum moves while the mesh remains fixed, which results in less resolution of details in the flow and a less precise definiton of interfaces but allows for large deformations. [38, 39] In the case of Fluid-Structure Interaction (FSI) problems, both the deformation of a solid structure, the flow field and the interface between both has to be modelled. Therefore, a combination of the Lagrangian and Eulerian description is used called the Arbitrary Lagrangian-Eulerian (ALE), which allows for arbitrary mesh movement. In the context of FSI, the solid can be described with the Lagrangian approach, while the majority of the fluid is modelled in a Eulerian way. [38–40] The arbitrary movement of the mesh can be applied to couple the Lagrangian description of the moving interface to the Eulerian description of the moving fluid.

2.6.2 Fluid dynamics solver

To model the fluid dynamics, the unsteady incompressible Navier-Stokes equations are solved [41]:

$$\rho_l \left(\frac{\partial \vec{v}_l}{\partial t} + (\vec{v}_l \cdot \vec{\nabla}) \vec{v}_l \right) - \vec{\nabla} \cdot \vec{\sigma}_l = \vec{f}, \tag{2.11}$$

$$\vec{\nabla} \cdot \vec{v}_l = 0, \tag{2.12}$$

where ρ is the density of the fluid, $\vec{v}_l$ represents the velocity, $\vec{f}$ is the body force per unit density and $\vec{\sigma}_l$ is the stress tensor given by:

$$\vec{\sigma}_l = 2\mu_l \vec{\epsilon} - p_l \boldsymbol{I}. \tag{2.13}$$

Here, μ_l and p_l represent the dynamic viscosity and pressure, respectively. $\boldsymbol{I}$ is the identity matrix. The strain rate tensor ϵ is defined as:

$$\vec{\epsilon} = \frac{1}{2} \left(\vec{\nabla} \vec{v}_l + (\vec{\nabla} \vec{v}_l)^T \right). \tag{2.14}$$

Since we are describing the fluid dynamics in an ALE framework, the convective term in the incompressible Navier-Stokes equation has to be modified to take into account the mesh velocity $\vec{v}_m$. The ALE formulation of the Navier-Stokes equation becomes [40]:

$$\rho_l \left(\frac{\partial \vec{v}_l}{\partial t} + (\vec{v}_l - \vec{v}_m) \cdot \nabla \vec{v}_l \right) - \vec{\nabla} \cdot \vec{\sigma}_l = \vec{f}, \tag{2.15}$$

$$\vec{\nabla} \cdot \vec{v}_l = 0. \tag{2.16}$$

2.6.3 Hyperelastic solid dynamics solver

The solid dynamics of the elastic walls is modelled in a Lagrangian framework meaning that the mesh moves along with the solid particles. Therefore, we have to distinguish between two coordinates systems: the initial and updated solid coordinate system. The material coordinate in the initial and updated system are $\vec{X}$ and $\vec{x}$, respectively. The mapping from the original Lagrangian framework to the updated coordinate system is given by $\vec{\phi}(\vec{X}, t)$ and the displacement of the solid particles can be written as: $\vec{u} = \vec{x} - \vec{X}$. The deformation gradient and the corresponding Jacobian determinant are defined as: $\vec{F} = \vec{\nabla}_X \vec{\phi}$ and $J = \det(\vec{F})$, respectively. [42, 43] Using these definitions, the momentum and continuity equation for the dynamics of the solid are given by [42]:

$$\rho_s \frac{\partial^2 \vec{u}}{\partial t^2} - \vec{\nabla}_x \cdot \vec{\sigma}_s = 0, \tag{2.17}$$

$$\rho_s J = \rho_{s0}. \tag{2.18}$$

with $\vec{\sigma}_s$ the symmetric Cauchy stress tensor, ρ_s the updated solid density and ρ_{s0} the initial density of the solid.

The hyperelasticity of the elastic walls is modelled using the model described in [42]. Here, they consider Neo-Hookean behaviour of the elastic material. Moreover, they decompose both the stress tensor and the Helmholtz free energy function into its deviatoric and volumetric parts. This yields the following system of equations to be solved for the hyperelastic solid:

$$\rho_s \frac{\partial^2 \vec{u}}{\partial t^2} - \vec{\nabla}_x p_s - \vec{\nabla}_x \cdot \mathrm{dev}[\vec{\sigma}_s] = 0, \tag{2.19}$$

$$\vec{\nabla}_x \cdot \vec{u} - \frac{1}{\kappa} p_s = g, \tag{2.20}$$

where p_s, κ and g represent the solid pressure, bulk modulus and the source term, respectively. $\mathrm{dev}[\vec{\sigma}_s]$ stands for the deviatoric part of the stress tensor.

2.6.4 Variational multiscale stabilized (VMS) finite element method

A variational multiscale stabilized (VMS) finite element method, as described in [41], is used to solve both the incompressible Navier-Stokes equation and the solid dynamics equations. In this method, the solution for the velocity, displacement and pressure fields are decomposed into coarse and fine scale components. First, the fine scale problems are approximated using the coarse scale residuals. The fine scale solutions are subsequently substituted into the coarse scale problem leading to an implicit modelling of the fine scale effects. This yields additional stabilization parameters, which results in an enhanced stabilization of the solutions. [41–43]

2.6.5 Mesh movement

In this work, the fluid mesh velocity at the solid boundary is set equal to the solid velocity, as calculated by the solid solver, following the Lagrangian approach. Far away from the boundary, the fluid can be described in a Eulerian manner implying no mesh deformation. In the vicinity of the fluid-structure boundary, an arbitrary mesh movement is applied. The mesh velocity in this region is calculated by 'diffusing' the mesh velocity at the fluid-structure interface, which is known as Laplace smoothing. This implies that the mesh movement will decrease as the distance to the boundary increases. The equation for Laplace smoothing is given by [40]:

$$\vec{\nabla} \cdot (\gamma \vec{\nabla} \vec{v}_m) = 0, \tag{2.21}$$

where $\vec{v_m}$ represents the mesh velocity and γ the mesh diffusion coefficient.

Various expressions can be used for the mesh diffusion coefficient γ. When γ is taken to be constant, Equation 2.21 reduces to the Laplace equation. However, this can cause mesh distortion since the mesh deforms mostly near the solid boundary. To overcome this problem, γ can be a function of the distance from a moving boundary. The diffusion coefficient can, for example, be taken inversely proportional to either the distance or the distance squared. [40, 43] In this work, a constant γ was used for the first implementation. In the future, this can be improved by implementing a distance-dependent γ.

2.6.6 Fluid-Structure interaction

The coupling between the fluid and the solid structure is done in a partitioned manner. This implies that the solid and the fluid equations are solved independently. Subsequently, the following coupling conditions are applied at the fluid-solid interface [43]:

$$\begin{aligned} \vec{v}_l &= \frac{\partial \vec{u}}{\partial t}, \\ \vec{\sigma}_l \cdot \vec{n} &= \vec{\sigma}_s \cdot \vec{n}, \end{aligned} \tag{2.22}$$

where $\vec{n}$ is the normal vector of the fluid-solid boundary.

These coupling conditions can be applied using either strong or weak coupling. Using strong coupling, sub-iterations are performed between the fluid and the structure until the conditions in Equation 2.22 are satisfied with a given tolerance before moving to the next timestep. [40, 43] In the case of weak coupling, no sub-iterations are performed. The coupling conditions are imposed once per timestep at the solid-fluid interface making this coupling formulation less computationally expensive. However, the coupling conditions are not necessarily satisfied, which might lead to instabilities. [44] In this work, no unexpected pressure oscillations were witnessed in the fluid domain when using weak coupling. Therefore, weak coupling was deemed sufficient for the FSI interaction.

3 | Methods

3.1 Monodisperse bubble production

We performed experiments using lipid-coated monodisperse bubbles, which were produced in-house using a custom-made microfluidic flow-focusing device shown in Figure 3.1a. The device produces microbubbles by focusing a gas thread between two liquid flows through a narrow aperture. The gas flow destabilizes causing monodisperse bubbles to be pinched off from the gas thread. After pinch-off the microbubbles decrease in size by a factor of 2-3 before they reach their final stable size. [45, 46]

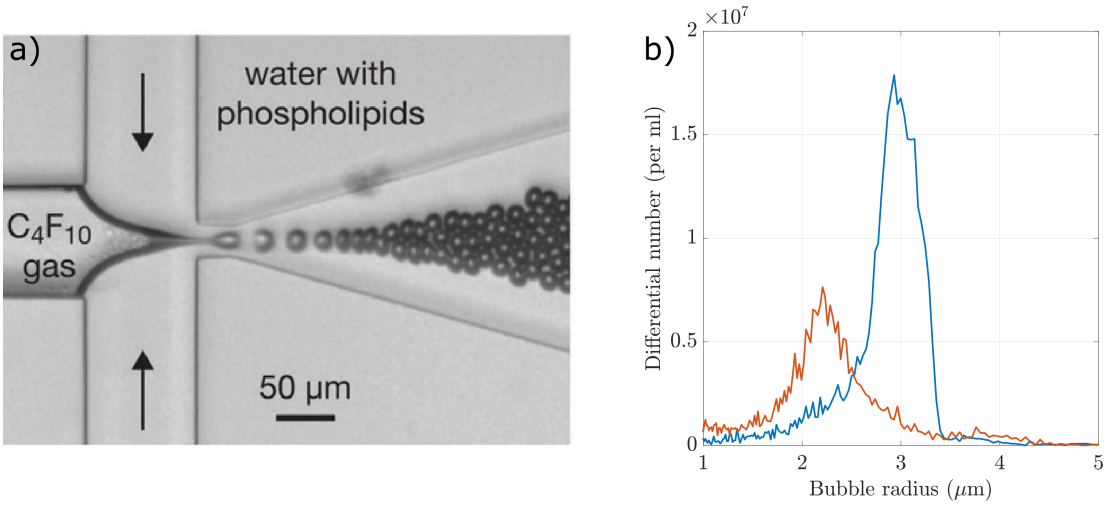

Figure 3.1: (a) Image of monodisperse microbubble production by flow-focusing device obtained from Segers et al. [45]. (b) Size distributions of two monodisperse bubble populations measured using a Coulter counter.

The phospholipids for the microbubble shell are contained in the aqueous phase. Before the microbubble pinch-off, the phospholipids adsorb onto the gas-liquid interface forming a monolayer. [46] The gas phase consists of a mixture of C_4F_{10} and CO_2. The high solubility of CO_2 and low solubility of C_4F_{10} result in an efflux of CO_2 out of the bubble leaving a stable microbubble filled with nearly pure C_4F_{10} gas without foam formation. [46, 47] The size of the microbubbles can be tuned by changing the flow rate and gas pressure. Before performing measurements with the microbubbles, the size distribution of the monodisperse bubbles was measured using a Coulter counter to determine the mean radius of the bubbles and to check the monodispersity. The size distributions of the two bubble populations used in the experiments are shown in Figure 3.1b.

3.2 Experimental setup

We built the experimental setup, as shown in Figure 3.2a, to observe the microbubble dynamics in a capillary both optically and acoustically.

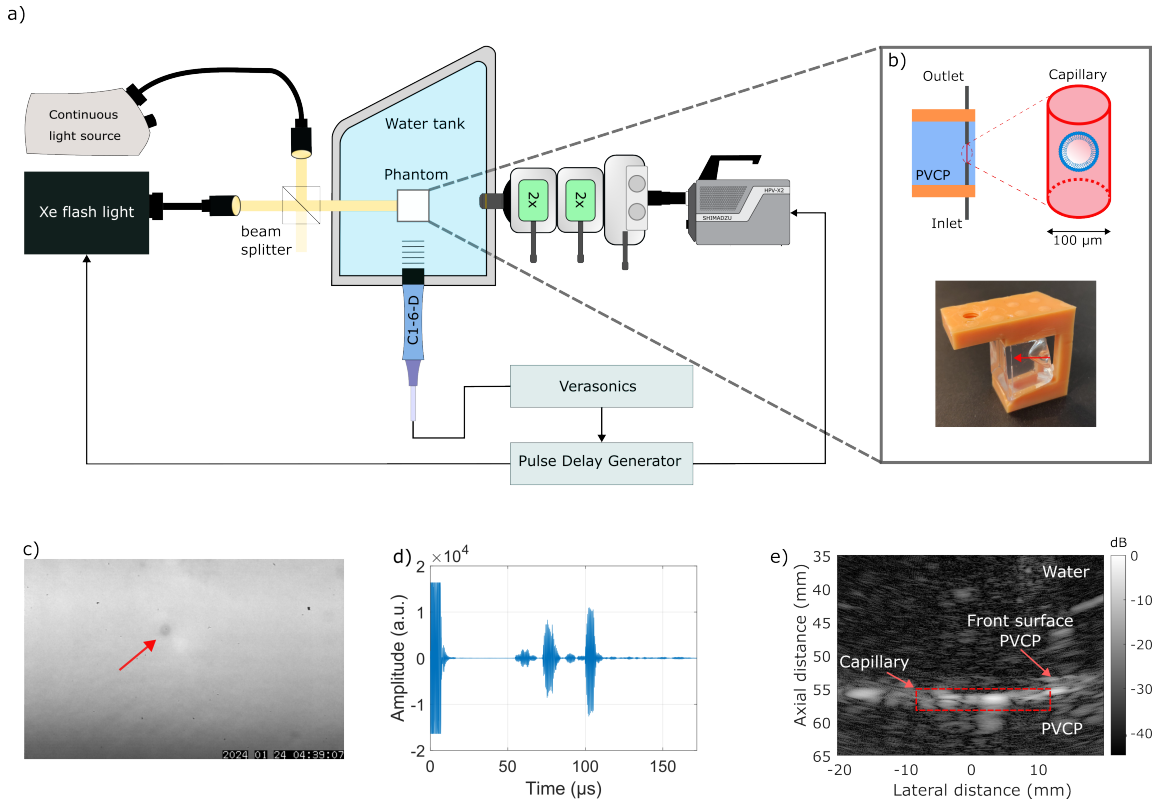

Figure 3.2: (a) Schematic of experimental setup. (b) Schematic (top) and image (bottom) of the capillary phantom. The red arrow points towards the location of the capillary. (c) Image of a microbubble (indicated by the red arrow) inside the capillary phantom obtained using the Shimadzu high speed camera. (d) Typical RF-line obtained by a single transducer element. (e) Reconstructed ultrasound image of the capillary phantom. The red dashed box indicates the location of the capillary.

A capillary phantom, shown in Figure 3.2b, was mounted on a 3-axis stage and positioned in a water tank filled with degassed water. A microscope with a 20x objective (Olympus SLMPlan N20x/0.25) was connected to either the Shimadzu HPV-X2 high speed camera to record the microbubble oscillations at 10 million frames/s, or to the Photron NOVA S16 camera to observe the microbubbles at a larger time scale at 16000 frames/s. Figure 3.2c shows an image of a microbubble inside the capillary phantom obtained using the high speed camera. The phantom was illuminated from the left by two light sources: a continuous light source (Schott KL 2500 LED) and a Xenon flash light (Vision Light Tech A-260 CE 10Hz). A beam splitter directs 50% of the light from each light source towards the phantom. The Xenon flash light is used during high frame rate measurements. The Xenon Strobe light emits an intense light flash with a duration of about 10 to $15\,\mu s$ yielding enough light for the high speed camera to record at 10 million frames/s. Due to the short duration of the light pulse, the continuous light source was needed to have a live view of the capillary while performing experiments. The GE C1-6D ultrasound transducer was positioned through an opening at the front side of a water tank, which was sealed by cling film. The transducer was oriented vertically to ensure a uniform

acoustic pressure over the entire region of the capillary.

To ensure the Xenon flash light and high speed camera were activated during microbubble oscillations, we created a trigger system. We connected a pulse delay generator (Berkeley Nucleonics Corporation 577-4C) to the Verasonics hardware system, the high speed camera and the flash light source, as depicted in Figure 3.2a. Once the ultrasound transducer started transmitting the chosen ultrasound waveform, the Verasonics sent a trigger to the delay generator. The signal was delayed by $40\,\mu s$ before activating the light source and a delay of $44\,\mu s$ was applied before triggering the camera to record to synchronize the arrival of the ultrasound wave at the capillary with the optical recording.

The GE C1-6D ultrasound transducer was used to both transmit the ultrasound waveforms and receive the acoustic response. A typical measured RF-line from the capillary phantom is shown in Figure 3.2d. The peak around $100\,\mu s$ corresponds to the reflection of the ultrasound wave at the back surface of the capillary phantom. The peak around $75\,\mu s$ is due to the reflection at the front surface of the PVCP, reflection at the capillary walls and scattering from microbubbles inside the capillary. Image reconstruction of the received RF data was performed using the delay-and-sum formulas 2.7 to 2.10, derived in section 2.4. Figure 3.2e shows a reconstructed image denoting the key elements in the image.

3.3 Characterization of GE C1-6D probe

In this study, we used the GE C1-6D transducer together with the programmable Verasonics Vantage 256 research ultrasound system for both transmitting and receiving ultrasound signals during measurements. The GE C1-6D is a curved array transducer with a center frequency around $3.4\,\mathrm{MHz}$ and a bandwidth ranging from around 1 to $6\,\mathrm{MHz}$. The probe has 192 transducer elements of which only the 56 center elements were activated for the measurements, while the remaining outer elements were inactivated. [48] Several ultrasound waveforms were used in the experiments for studying the bubble dynamics. A zero-time delay was applied between the transducer elements leading to the emission of unfocused, slightly diverging plane waves. In order to compensate the measured radio frequency (RF) signals for the transducer characteristics, the transmit and receive characteristics of the C1-6D ultrasound transducer were determined.

Transmit characteristics

The transmit characteristics of the different waveforms were determined in a characterization experiment. Figure 3.3a shows a schematic of the characterization setup. The probe was positioned horizontally through an opening at the front side of a large water tank, which was sealed by cling film. In the water tank, a fibre optic hydrophone (FP188-13, Precision Acoustics) was placed to measure the ultrasound pressure at different distances and positions relative to the probe. The translation of the hydrophone was achieved by attaching it to a 3-axis translational stage. The X, Y and Z-direction correspond to the axial, lateral and elevational direction, respectively, as depicted in Figure 3.3a. The hydrophone scanned three different planes to determine the elevation, lateral and axial focus. An XY-plane of 10 by 20 mm, an YZ-plane of 40 by 10 mm and an XZ plane of 10 by 10 mm were scanned around the expected focus of the transducer. The step size in the X, Y and Z-direction were taken to be 0.25 mm. One exception was the smaller step size of 0.125 mm in the X-direction when scanning the XY-plane. Thirteen different ultrasound pulses were characterized. The first type of

pulse was a broadband pulse of a single cycle with a frequency of $2\,\mathrm{MHz}$. Besides, a down-chirp, which is a frequency modulated signal with a decreasing frequency over time, was transmitted by the ultrasound transducer. The chirp frequencies ranged from $6\,\mathrm{MHz}$ down to $1\,\mathrm{MHz}$. Moreover, 11 narrowband pulses with a pulse length of 10 cycles were emitted and characterized using the hydrophone. These narrowband waveforms had a frequency ranging from $1\,\mathrm{MHz}$ to $6\,\mathrm{MHz}$ in steps of $0.5\,\mathrm{MHz}$ to cover the entire bandwidth of the transducer. The peak amplitude of the waveforms was set to $4\,\mathrm{V}$. To synchronise the hydrophone measurement with the transmit of the ultrasound pulse, the Verasonics ultrasound system sent a trigger to the picoscope (PicoScope 5000 Series) upon transmit of the pulse. Each waveform was repeated 50 times and the measured signal was averaged over the repeats.

The pressure amplitudes measured by the hydrophone were corrected for the transmit voltage to obtain the pressure/voltage. The pressure field obtained for the XZ-plane using the narrowband pulse of $3\,\mathrm{MHz}$ is shown in Figure 3.3b. The XY- and YZ-planes are included in Appendix A.1. From this pressure map, it can be seen that the peak pressure at the elevation and axial focus is between 25 and $30\,\mathrm{kPa/V}$.

We determined the transmit characteristics of the transducer for the chirp and the narrowband pulses, separately. These were determined based on the 49 pressures measured around the center of the XZ-plane, depicted by the red square in Figure 3.3b. In case of the chirp, the pressure amplitudes were averaged and plotted as a function of frequency. Moreover, the pressure amplitudes were corrected for the voltage tri-state transmitted by the ultrasound transducer to obtain the pressure output per voltage. The obtained transmit curves, before and after compensating for the transmitted voltage tri-state, were smoothed resulting in the curves shown in Figure 3.3c and d, respectively. For each of the narrowband pulses, the mean pressure amplitude was calculated at the transmit frequency of the pulse. Combining the pressure amplitudes of all pulses and plotting against the corresponding transmit frequencies resulted in a transmit curve similar to the one obtained for the chirp, as can be seen in both Figure 3.3c and d.

Receive and transmit-receive characteristics

The transmit-receive (TR) characteristics for a fundamental and harmonic response were determined using the acoustic response from an alignment phantom, consisting of an electrical wire surrounded by PVCP. This acoustic response, measured after transmission of a chirp, is shown by the blue curve in Figure 3.3e. It represents the TR-characteristics for a fundamental response since the wire is a linear scatterer. We can write this linear acoustic response by a convolution of the transmit and receive characteristics of the probe. The harmonic response, i.e. the response at twice the transmitted frequency, is estimated by convolving the transmit characteristics with the receive characteristics at twice the transmit frequency. These convolutions are summarized in the equations below:

$$TR_{\mathrm{fund}}(f) = T(f) \cdot R(f), \tag{3.1}$$

$$TR_{\mathrm{harm}}(f) = T(f) \cdot R(2f), \tag{3.2}$$

where $TR_{\mathrm{fund}}(f)$ and $TR_{\mathrm{harm}}(f)$ are the transmit-receive characteristics of the fundamental and harmonic response for a transmit frequency f, respectively. $T(f)$ represent the transmit characteristics as a function of transmit frequency. $R(f)$ and $R(2f)$ are the receive characteristics at once or twice the transmit frequency, respectively.

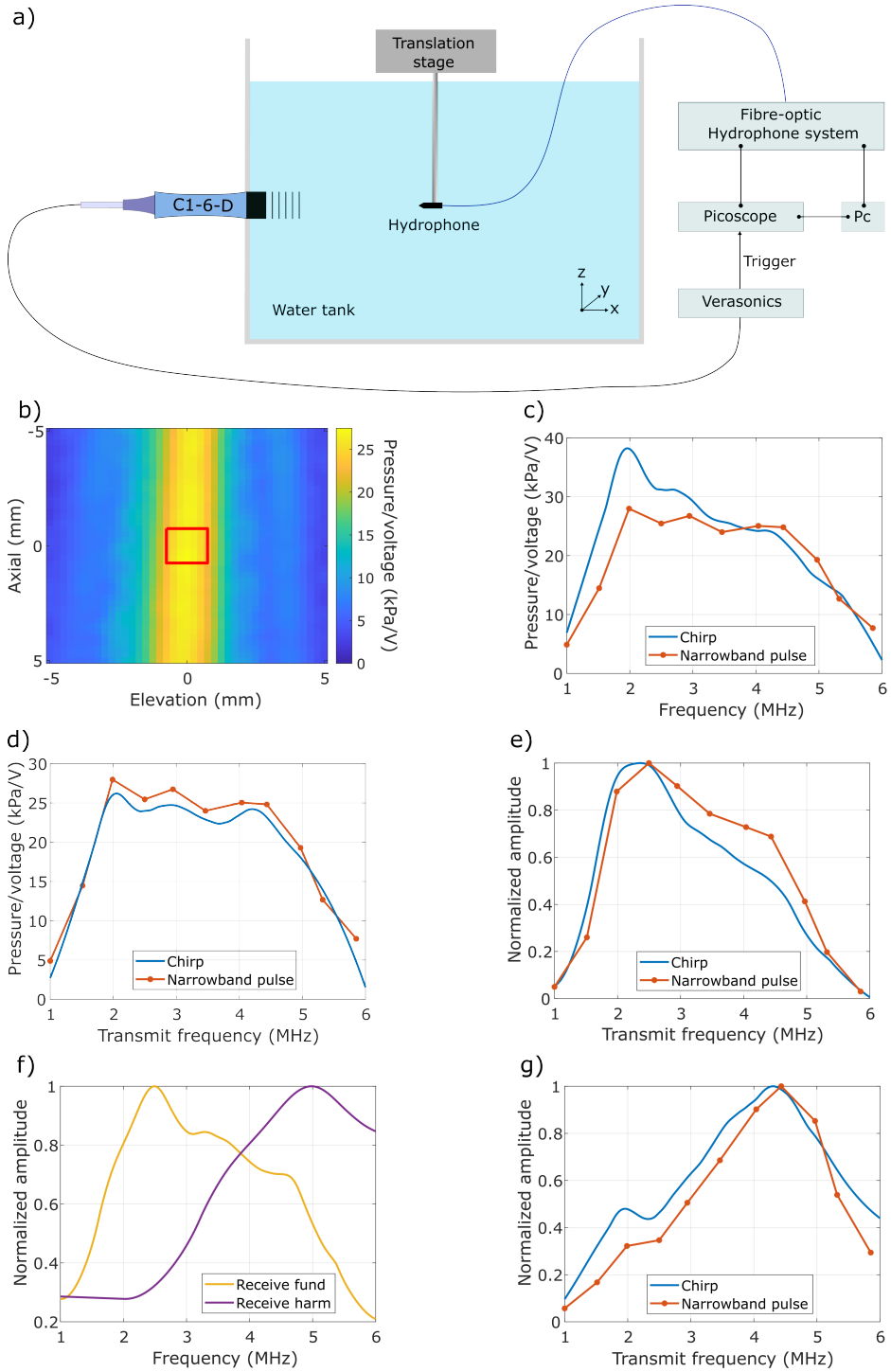

Figure 3.3: (a) Schematic of setup used for characterizing the GE C1-6D ultrasound probe. (b) The XZ pressure field measured by the hydrophone for a narrowband pulse of $3\,\mathrm{MHz}$ transmitted by the C1-6D probe. (c) Transmit characteristic curve of the C1-6D probe for a chirp and narrowband pulses as a function of transmit frequency. The transmit of the chirp is not compensated for the voltage tri-state transmitted by the ultrasound transducer. (d) Transmit characteristic after compensating for the voltage tri-state. (e) Transmit-receive characteristics for a fundamental response of a chirp and narrowband pulses. (f) Receive characteristics for the fundamental and harmonic response of a chirp and narrowband pulses. (g) Transmit-receive characteristics for a harmonic response of a chirp and narrowband pulses.

To obtain the TR-characteristics for the narrowband pulses and for harmonic responses, we determined the receive characteristics. The fundamental receive characteristics were obtained by dividing, in the Fourier domain, the measured signal from the alignment wire by the transmit characteristics of the chirp. Figure 3.3f shows the fundamental receive characteristic curve. By multiplying the fundamental receive with the transmit characteristics of the narrowband pulses, according to Equation 3.1, the fundamental reference signal for the narrowband pulses was determined. Figure 3.3e shows this reference signal together with the measured reference response for the chirp. The harmonic response is at twice the transmit frequency. Therefore, the harmonic receive characteristic as a function of transmit frequency is shifted to the right and scaled with respect to the fundamental receive, as shown in Figure 3.3f. Substituting this harmonic receive characteristic and the transmit characteristics into Equation 3.2, the TR-characteristics for the harmonic response of the chirp and the narrowband pulses were determined. These are shown in Figure 3.3g.

3.4 Ultrasound waveforms

In the experiments, several types of ultrasound waveforms were transmitted by the GE C1-6D ultrasound transducer: a broadband imaging pulse of 1 cycle, narrowband imaging pulses of 10 cycles and a $15\,\mu s$ down-chirp. To ensure that both the fundamental frequency and the second harmonic would fall within the bandwidth of the transducer, the transmit frequencies of the imaging pulses were chosen to be below $3\,\mathrm{MHz}$. The ultrasound frequency of the broadband imaging pulse was chosen to be $2\,\mathrm{MHz}$. The narrowband imaging pulses were transmitted at 1.5, 2.0 and $2.5\,\mathrm{MHz}$. The frequency of the down-chirp ranged from $6\,\mathrm{MHz}$ down to $1\,\mathrm{MHz}$ to cover the full transducer bandwidth. The Verasonics Vantage software system simulated the transmitted waveforms. These simulated waveforms together with the corresponding Fast Fourier Transforms (FFTs) are shown in Figure 3.4.

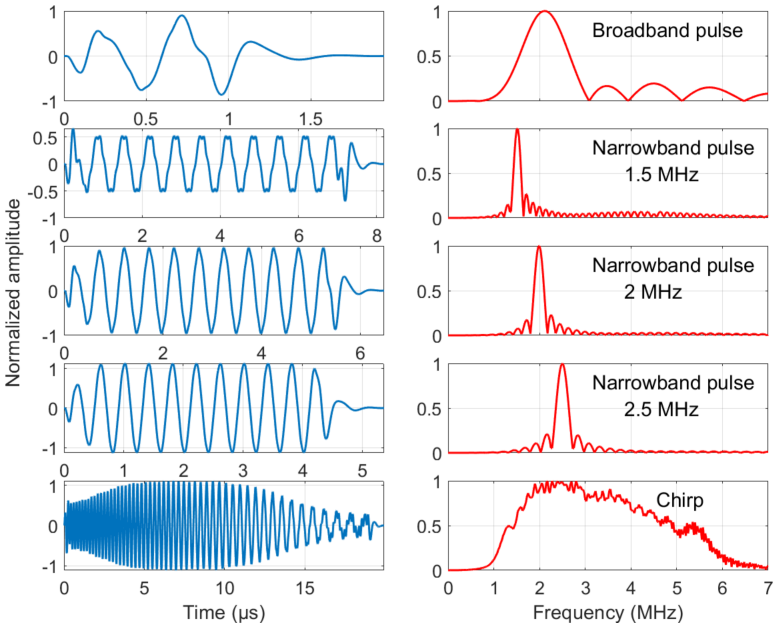

Figure 3.4: Ultrasound waveforms used in experiments. (Left) Waveforms as simulated by the Verasonics Vantage software system. (Right) Fast Fourier Transforms corresponding to the waveforms shown on the left.

Pulse inversion was used to distinguish the fundamental responses from the harmonic responses. The time between the transmission of the upright and the inverted waveform was set to $200\,\mu s$. A smaller value was not feasible due to the response time of the Verasonics and the two-way traveltime of the waveforms. Using a flow rate of $100\,\mu L/min$ and a capillary with a diameter of $100\,\mu m$, this implied that the microbubbles or beads moved about $0.04\,mm$ in between PI acquisitions. Therefore, the moving particles could be assumed to be stationary. The transmit voltage was set to $9\,V$ for the broadband imaging pulse and $4\,V$ in case of the chirp and the narrowband pulses. These voltages corresponded to a peak pressure of about 100 to $120\,kPa$, as can be determined from Figure 3.3b.

3.5 Capillary phantom

We used a 3D-printed mold to produce the small capillary phantoms. We inserted needles through the top and the bottom of the mold. A fishing thread or tungsten wire with the desired diameter of the capillary was passed through the needles. Next, polyvinyl chloride plastisol (PVCP), obtained from Bright Baits, was degassed in a vacuum pump for several minutes. Thereafter, it was heated up in the microwave causing the PVCP to transition from a white milky solution into a transparent liquid. With the wire in place, we filled the mold with the heated PVCP. After the PVCP had hardened into a viscoelastic gel, we gently pulled the wire out of the gel to create a hollow capillary with the desired diameter and a length of about 5 to $10\,mm$. Figure 3.2b shows a schematic and a real image of the phantom. In the experiments, we used a capillary with a diameter of $100\,\mu m$. The capillary was located in the corner of the mold, 2 mm from the front and right surface of the phantom. The ultrasound waves thus had to transverse only 2 mm of PVCP to reach the capillary minimising the amount of ultrasound attenuation. Moreover, since the distance between the right surface and the capillary was also 2 mm, less light was scattered leading to better optical images. The capillary had a vertical orientation inside the gel phantom to prevent microbubbles from floating towards the wall of the capillary during perfusion. Since the steel needles highly reflected the ultrasound waves, we replaced them by plastic tubing. The tubing was connected to a syringe on a syringe pump (PHD 2000, Harvard Apparatus) to enable flow through the capillary. The flow was directed upwards through the capillary in accordance with the floating direction of the bubbles and the beads. A magnetic stirrer was used to keep the microparticles diffused and dissolved in the solution.

3.6 Experimental protocol

First, we aligned the optical and acoustical system using an alignment phantom. Figure 3.3b shows the importance of this alignment, as the elevation focus spans about $1\,mm$ in width. The alignment phantom was similar to the capillary phantoms, except with an electric wire replacing the capillary. With the alignment phantom in the water tank, the transducer continuously transmitted and received short ultrasound pulses at $2\,MHz$ with a time of $200\,ms$ between each pulse. The received RF-lines corresponding to the eight center elements were averaged and plotted. We adjusted the relative position of the wire with respect to the transducer until the measured RF-lines showed a maximum reflection signal from the wire. This implied that the wire was in the elevation focus of the transducer. Next, we adjusted the position of the microscope until the wire was in the optical focal region ensuring that the elevation focus overlapped with the optical focal region.

Once the optical and acoustical focus were aligned, we replaced the alignment phantom by a capillary phantom. First, the phantom was perfused with deionised, filtered water. A pre-measurement was

performed with a narrowband imaging pulse to check the saturation of the signal. Again, the average of the received RF-lines were plotted. The value for the Time Gain Compensation (TGC) was adjusted until the RF-signal reached its maximum without being saturated. Thereafter, we performed measurements with either no scatterers, hollow glass beads or monodisperse microbubbles present inside the capillary. The monodisperse microbubbles had a radius of $2.2\,\mu\mathrm{m}$ or $2.9\,\mu\mathrm{m}$. The size distribution of these microbubbles is given in Figure 3.1b. These scatterers were perfused through the capillary at a flow rate of $100\,\mu\mathrm{l/min}$. This corresponded to a velocity of $0.2\,\mathrm{m/s}$ in a capillary with a diameter of $100\,\mu\mathrm{m}$. For each type of scatterer, the acoustic response was determined for the several ultrasound waveforms, discussed in section 3.4. The ultrasound transducer transmitted and received a sequence of 600 pulses, comprising an upright and inverted pulse, for each ultrasound waveform at a rate of 10 pulses per second. The RF signals obtained without scatterers and with hollow glass beads were used as a baseline control and for linear reference, respectively.

3.7 Data Processing

The received ultrasound signals were processed using Matlab. First, pulse inversion was applied to all signals to separate the fundamental and harmonic response. For the analysis of frequency components in the measured signals, the Fast Fourier Transform (FFT) was used. Additionally, ultrasound images were reconstructed from the RF data.

3.7.1 Delay-and-sum ultrasound image reconstruction

Before reconstructing the time signals in the RF data to a 2D image, the Fast Fourier Transform (FFT) of the RF data was calculated to apply Fourier filtering. Since the negative frequencies in the spectrum contain the same information as the positive frequencies, the amplitude of the positive frequencies were doubled, while the negative frequencies were removed. Next, we filtered out frequencies above $10\,\mathrm{MHz}$ and below $0.5\,\mathrm{MHz}$ to reduce noise in the images. Subsequently, the inverse Fourier Transform was used to obtain the filtered RF data. Each column of the filtered RF data contains the time signal measured by a transducer element. These time signals can be related to a spatial location using delay-and-sum beamforming based on the two-way travel time of the waveform, as described in section 2.4. By determining the time signals corresponding to each pixel in the imaging plane, a 2D image was formed. Subsequently, image demodulation was used to obtain the envelope of the signals. Finally, the image was converted to a dB scaled image using log compression. In this thesis, the RF data received when transmitting the broadband pulse was used for image reconstruction since this waveform yields the best resolution due to its shorter pulse length.

3.7.2 Pulse inversion

To determine the effectiveness of using pulse inversion, the ultrasound signals scattered from an electrical wire, hollow glass beads and microbubbles were compared. Here, the electrical wire and beads act as linear scatterers, whereas the microbubbles are nonlinear scatterers. Both an upright and inverted narrowband pulse at a frequency of $2\,\mathrm{MHz}$ were transmitted. The RF data obtained from the pulse inversion (PI) acquisitions were combined. The RF data retrieved from the upright and inverted waveform were subtracted and summed to split the data into the fundamental and harmonic responses, respectively, according to Equation 2.3. The measurements for the different scatterers were performed using the same value for the TGC.

3.7.3 Frequency analysis

After applying pulse inversion, the frequency spectra of the fundamental and harmonic responses were obtained. Since we are interested in the signal originating from the location of the capillary or electrical wire, spatial filtering was applied. The RF data of a single frame was reconstructed into an image. In the reconstructed image, a region of interest (ROI) around the location of the capillary or wire was selected. Using the delay-and-sum formulas in section 2.4, the time delays of the signal originating from the ROI in the image are determined. The rows in the RF data corresponding to these time delays were selected, while the remaining rows were removed. Thereafter, the frequency spectrum of the filtered RF data was calculated using the Fast Fourier Transform (FFT). Finally, the frequency spectra were compensated for the transmit-receive characteristics of the transducer. This was done by dividing the fundamental and harmonic frequency spectra by the reference response signals of the transducer, as shown in Figure 3.3e and g.

3.8 Simulation model

3.8.1 Structured and unstructured mesh

Figure 3.5a shows the geometry of the simulation. The inside of the capillary was represented by a rectangular fluid domain with a length of $1\,\mathrm{mm}$ and a width of $0.1\,\mathrm{mm}$. In the center of the fluid domain a circular void was created with a radius of $0.002\,\mathrm{mm}$ simulating a microbubble. The left and right side of the fluid domain were attached to rectangular elastic solid domains with a thickness of 0.01 mimicking the capillary walls. A zoom-in on the geometry and the mesh used for the simulations are shown in Figure 3.5b and c. The mesh was generated using the finite element mesh generator Gmsh version 4.11.1. A combination of an unstructured and structured mesh was used. Structured meshes were used for the solid and in the region surrounding the microbubble since these regions have a regular shape. The remainder of the fluid was described with an unstructured mesh, which is adaptable to any shape. The elements within the elastic walls had a uniform size, while the element size in the fluid domain increased with the distance from the bubble wall. This resulted in a fine mesh near the boundary of the bubble and a coarser mesh in the bulk fluid reducing the computational expense.

3.8.2 Boundary conditions

In order to simulate the dynamics of the microbubble and its shell, the pressure terms on the right-hand side of the Rayleigh-Plesset equation, as given in Equation 2.1, were set as a boundary condition on the bubble wall. The pressure term, $\frac{4\mu_l}{R}\frac{\mathrm{d}R}{\mathrm{d}t}$, corresponding to the energy dissipation due to the liquid viscosity was omitted since this dissipation was already accounted for when solving the fluid dynamics of the surrounding liquid. The acoustic driving pressure $P_A(t)$ was implemented as a sine wave with a constant ultrasound pressure amplitude. A list of the parameter values used in the simulation is given in Appendix A.2.

The bubble-radius-dependent surface tension, as described by the Marmottant model given in Equation 2.2, was modelled using the following equation:

$$\sigma(R) = \begin{cases} 0 & \text{if} \quad \sigma \leq 0 \\ \sigma_0 + \chi\left(\frac{R^2}{R_0^2} - 1\right) & \text{if} \quad 0 \leq \sigma \leq \sigma_{\text{water}} \\ \sigma_{\text{water}} & \text{if} \quad \sigma \geq \sigma_{\text{water}} \,. \end{cases} \tag{3.3}$$

At the inlet and outlet of the fluid domain, we set the pressure boundary condition equal to the atmospheric pressure. At the interface between the fluid and the elastic walls, we used the no-slip boundary condition for the velocity together with the coupling conditions given in Equation 2.22.

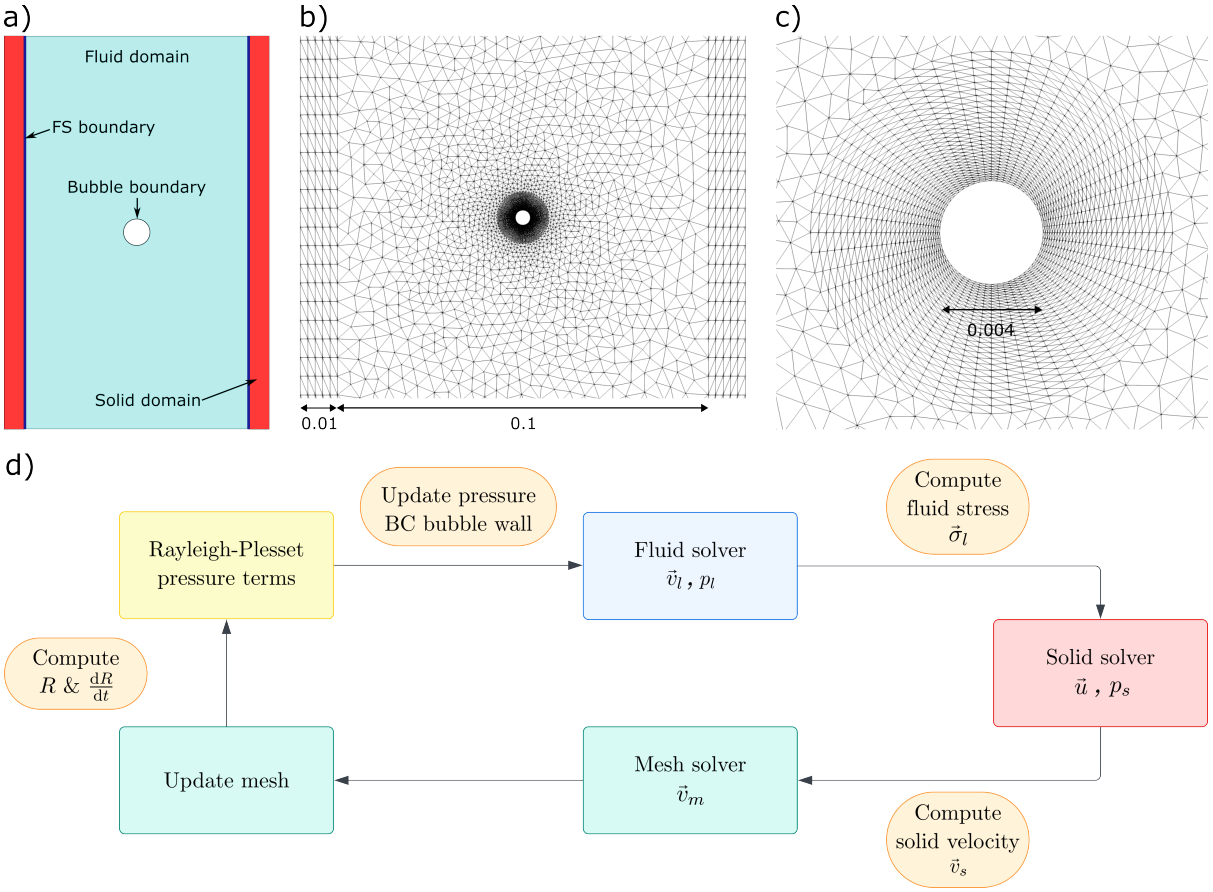

Figure 3.5: (a) Schematic of the simulation geometry. The fluid-solid (FS) boundary is depicted by the dark blue lines. (b) Mesh of part of the fluid and solid domain in the simulation. (c) Mesh zoomed in on the region around the bubble area. (d) Simulation scheme showing the different steps for a single iteration. The first iteration starts with determining the current radius of the bubble R.

3.8.3 Simulation scheme

Figure 3.5d shows a simulation scheme of the different steps in the simulation.
The first step in the simulation is to determine the current radius of the microbubble. At the start of the simulation the initial bubble radius is set to $2\,\mu\text{m}$. After one iteration, the bubble radius at each node on the bubble boundary is calculated using the following equation:

$$\vec{R}_t = \vec{R}_{t-1} + \vec{v}_{\text{bw}} \cdot \Delta t, \tag{3.4}$$

with $\vec{R}_t$ and $\vec{R}_{t-1}$ the bubble radius vector at the current and the former timestep, respectively, and Δt the timestep. $\vec{v}_{\mathrm{bw}}$ is the mesh velocity vector at the bubble wall, which is obtained from the fluid solver.

The average of $\vec{R}_t$ is calculated and used as the current bubble radius. Subsequently, the radial velocity of the bubble wall $\frac{\mathrm{d}R_t}{\mathrm{d}t}$ is calculated using a first-order explicit Euler-forward time-integration scheme:

$$\frac{\mathrm{d}R_t}{\mathrm{d}t} = \frac{R_t - R_{t-1}}{\Delta t}, \tag{3.5}$$

where R_t and R_{t-1} are the average bubble radii at the current and the former timestep, respectively.

Next, the pressure terms on the right-hand side of the Rayleigh-Plesset equation (Equation 2.1) are evaluated and set as a pressure boundary condition at the bubble boundary.

Using this boundary condition to describe the bubble dynamics, the Navier-Stokes equation (Equation 2.15) is solved by the fluid solver. The fluid stress is computed using Equation 2.13 and transported to the solid solver according to the second coupling condition in Equation 2.22. Thereafter, the solid solver solves the system of equations given in Equations 2.19 and 2.20 for the elastic walls yielding the solid displacement and pressure. The velocity of the solid $\vec{v}_{\mathrm{s}}$ is computed using an Euler-forward time-integration scheme:

$$\vec{v}_{\mathrm{s}} = \frac{\vec{u}_t - \vec{u}_{t-1}}{\Delta t}, \tag{3.6}$$

with $\vec{u}_t$ and $\vec{u}_{t-1}$ the current and the former displacement vector, respectively.

Afterwards, the solid velocity is transported to the fluid domain according to the first coupling condition in Equation 2.22. The mesh solver then 'diffuses' the fluid mesh velocity according to Equation 2.21, with the solid velocity as a boundary condition at the fluid-wall interface and the bubble wall velocity as a boundary condition at the fluid-bubble interface. Subsequently, the solid mesh is moved and the fluid mesh coordinates are updated according to this diffused mesh velocity. This causes both the bubble wall and the elastic wall to move together with their surrounding fluid cells.

After mesh movement of both the solid and fluid mesh, a single iteration has been completed. The radius and radial velocity of the bubble have been updated. Therefore, we go back to the first step in the simulation scheme to start the next iteration.

From a single simulation run, the evolution of the bubble radius over time can be extracted and the maximum amplitude of the radial oscillations can be calculated. By running the simulation for several ultrasound frequencies and computing the amplitudes of the bubble oscillations, the resonance curve of the bubble was determined.

4 Results

4.1 Spectral separation through pulse inversion

As described in section 3.4, pulse inversion (PI) was used to acquire the RF data, allowing for distinguishing the fundamental response from the harmonic response. Figure 4.1a shows the upright and inverted RF lines, measured after scattering from an electrical wire. The measured response of the upright and inverted waveform generated by the beads and the microbubbles in the capillary phantom are shown in Figure 4.1c and e, respectively. The RF data retrieved from the upright and inverted waveform were subtracted and summed to split the data into the fundamental and harmonic responses, respectively. This resulted in the waveforms shown in Figure 4.1b, d and f.

Figure 4.1b shows that the fundamental response from the electrical wire is doubled relative to the original signal, while the maximum harmonic signal amplitude is only about 3.5% of the fundamental signal, which is as expected for a linear scatterer. Due to nonlinear propagation, however, the signal retrieved from the linear scatterer also contains some nonlinearity causing the harmonic response to not vanish entirely. The linear beads generate a similar response, as shown in Figure 4.1d. The beads' signal shows some modulation due to interference of the scattered ultrasound waves, which is not observed for the wire response. The fundamental microbubble response is also doubled with respect to the upright and inverted RF signals, as can be observed from Figure 4.1f. However, the harmonic signal has a maximum amplitude around 5.5% of the fundamental RF signal, which is larger than for the wire and the beads. This increased harmonic response suggests that we measure the nonlinear response of microbubbles. However, other similar measurements show a lower harmonic response for the microbubbles than for the beads. The increased harmonic response observed for the microbubbles is thus most likely caused by nonlinear propagation effects as well.

The Fast Fourier Transform (FFT) of the RF data from the microbubbles and the wire was determined before and after using pulse inversion. For comparison, the FFT amplitudes were normalized with respect to the maximum amplitude in the frequency spectrum without applying pulse inversion. Figure 4.1g shows the obtained frequency spectra when no pulse inversion is applied. Here, peaks can be observed at the transmit frequency (i.e. $2\,\mathrm{MHz}$) and at twice the transmit frequency (i.e. $4\,\mathrm{MHz}$). The frequency spectra obtained after subtracting the RF data of the upright and inverted pulse are given in Figure 4.1h by the orange and yellow curve. In comparison to the frequency content without applying PI, the peak at twice the transmit frequency has disappeared while the fundamental frequency peak is still present. On the contrary, the harmonic frequency response is retained, while the amplitude at the fundamental frequency is reduced by a factor of about 200 after adding the upright and inverted response. This can be observed from the purple curve and red curves in Figure 4.1f. A small peak at the fundamental frequency is still present in the harmonic frequency spectrum because the inverted pulse transmitted by the ultrasound transducer is not the exact inverse of the upright pulse. Therefore, the linear response from the inverse and upright pulse don't cancel out entirely.

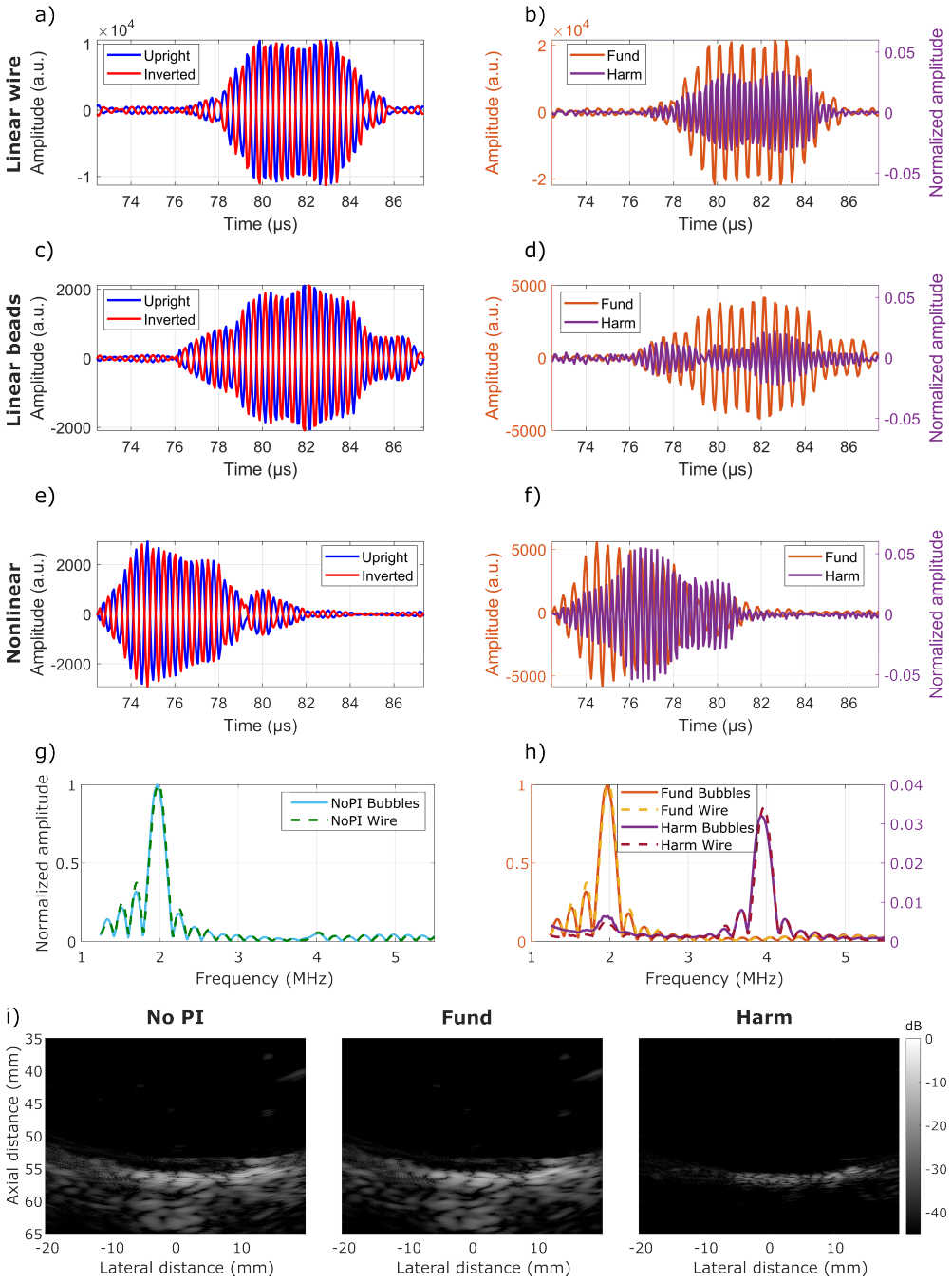

Figure 4.1: (a) Wire response to upright pulse and inverted pulse. (b) Fundamental and harmonic wire response. (c) Beads response to upright pulse and inverted pulse. (d) Fundamental and harmonic beads response. (e) Microbubble response to upright pulse and inverted pulse. (f) Fundamental and harmonic microbubble response. (g) Fast Fourier Transform (FFT) of microbubble and wire response without applying pulse inversion (PI). (h) FFT of fundamental and harmonic microbubble and wire response. (i) Reconstructed ultrasound images of microbubble scatter without applying PI (left). Reconstructed image of fundamental (middle) and harmonic (right) microbubble response.

The bottom row in Figure 4.1 shows the reconstructed ultrasound images corresponding to the measured microbubble response. No PI was applied for the left image. The middle and right image are reconstructed from the fundamental and harmonic data, respectively. The original reconstructed image (left) and the image showing the fundamental signal (middle) are very similar. This observation is as expected since the majority of the detected signal originates from fundamental scattering. The harmonic image shows signal predominantly originating from the region of the capillary because of the presence of both moving scatterers and nonlinear microbubbles inside the capillary. In the surrounding water and polyvinyl chloride plastisol (PVCP), the scatterers are purely linear causing them to be removed when applying PI. Moreover, it can be observed that the speckle size in the harmonic image is twice as small as the speckle size in the fundamental image since the harmonic ultrasound wavelength is half the fundamental wavelength.

4.2 Nonlinear microbubble response in capillary

To investigate whether the nonlinear microbubble response can be measured, the received ultrasound signals of the microbubbles were compared to the response from linear beads. The frequency spectra measured after transmission of a chirp and a narrowband pulse at $2\,\mathrm{MHz}$ are shown in Figure 4.2a to d for beads and microbubbles with a radius of $2.2\,\mu\mathrm{m}$ and $2.9\,\mu\mathrm{m}$. The frequency spectra corresponding to narrowband pulses with a transmit frequency of $1.5\,\mathrm{MHz}$ are given in Appendix A.3. The reconstructed ultrasound images with either microbubbles or beads perfused through the capillary phantom are shown in Figure 4.2e to h. Figure 4.2e and g show the fundamental images and Figure 4.2f and h show the harmonic images.

The acoustic frequency response measured for the hollow glass beads and the microbubbles is similar for both transmitted ultrasound waveforms. In case of the chirp, the maximum difference between the beads and microbubbles response is 0.9 dB and 2.4 dB for the fundamental and harmonic spectra, respectively. In the narrowband pulse spectra, the amplitude of the fundamental response generated by the beads is 7 dB lower while the harmonic response is only about 1 dB smaller than the microbubble response. This implies that the harmonic response is larger with respect to the fundamental response for the beads than for the bubbles. Further research is needed to determine the cause of this unexpected result.

A higher signal intensity is observed for the microbubbles in both the images and the frequency spectra for the narrowband pulses. This might be due to, for example, the higher effective scatter cross section of the microbubbles or a higher concentration of microbubbles than beads. The microbubbles show both a fundamental and harmonic response as expected for a nonlinear scatterer. However, the beads also show a significant harmonic response. Similarly, the reconstructed images based on the harmonic RF data show signal originating from the capillary region in case of both the beads and the microbubbles. Based on this observation, we conclude that the measured harmonic signal likely does not originate from the nonlinear microbubble response. Instead, the higher harmonic can most likely be attributed to nonlinear propagation effects. The measurements are, thus, not sensitive enough yet to distinguish the nonlinear bubble response from other sources of harmonic signal.

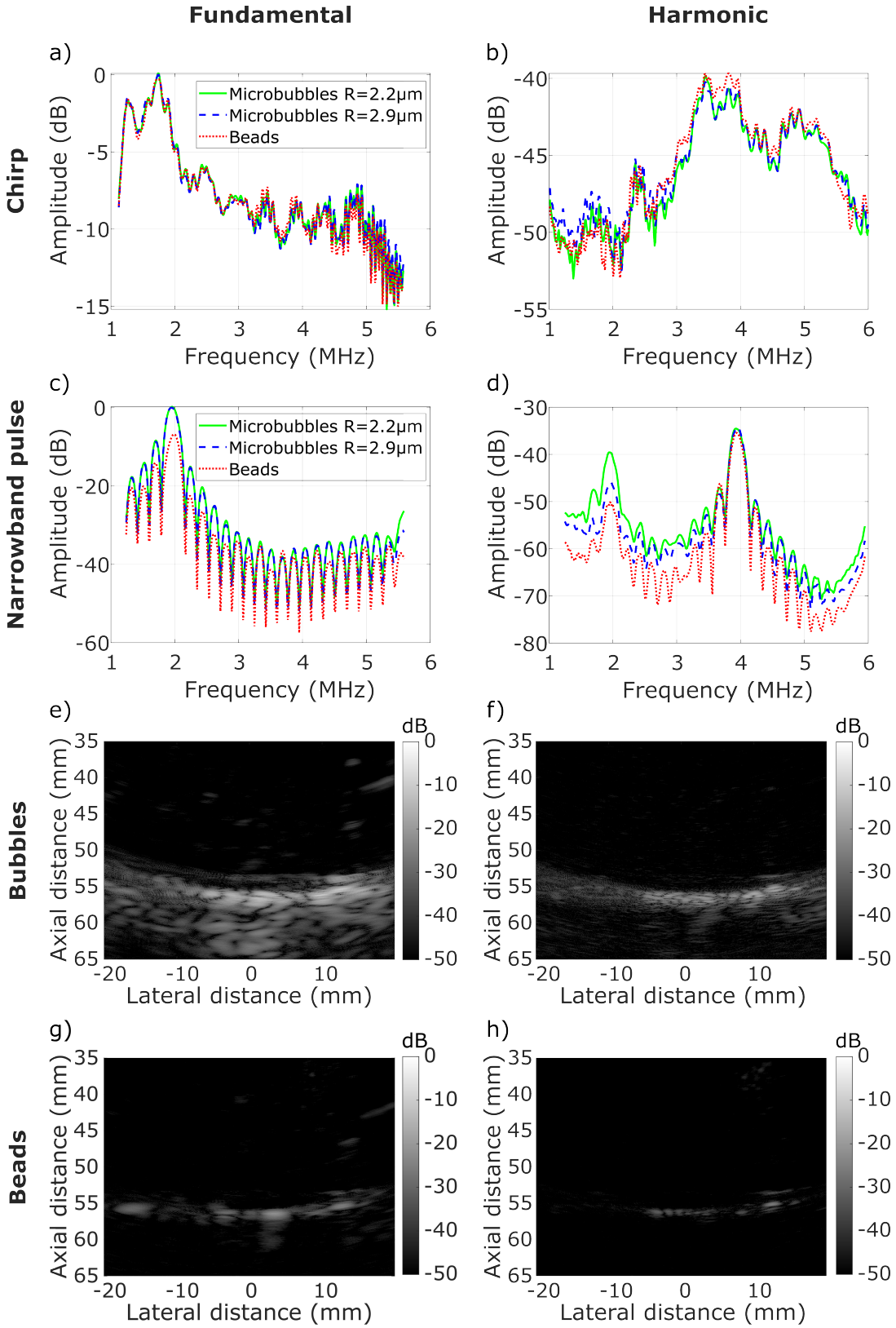

Figure 4.2: (Left) Results based on fundamental RF data. (Right) Results based on harmonic RF data. (a-b) Frequency spectra showing the response to a down-chirp with a frequency decreasing from $6\,\mathrm{MHz}$ down to $1\,\mathrm{MHz}$. (c-d) Frequency spectra showing the response to a narrowband pulse with a transmit frequency of $2\,\mathrm{MHz}$. (g-h) Reconstructed images with microbubbles present in the capillary phantom. (i-j) Reconstructed images with beads present in the capillary phantom.

4.3 Quantitative frequency analysis after SVD filtering

To distinguish the signal generated by the moving microbubbles and beads from the static tissue, we studied the use of Singular Value Decomposition (SVD) filtering. To compare the acoustic response of linear beads and nonlinear microbubbles at different ultrasound frequencies, a quantitative measurement of the amplitudes of the fundamental and harmonic frequency response is required. Here, we investigate the effect of SVD filtering on the frequency content of RF Data, measured after scattering from an electrical wire, hollow glass beads and microbubbles. We perform SVD filtering with several lower limits for the singular value ranging from 1 to 20 singular values. Here, a lower limit of 1 implies that no singular values are removed, i.e. no filtering, while a limit of 20 implies that the first 19 singular values are filtered out. The number of frames recorded determines the total count of singular values, which was 100 for the wire and 600 for the microbubble and beads measurements. After applying pulse inversion, the fundamental and harmonic RF data received using the narrowband pulses was SVD filtered for each singular value lower limit. Subsequently, a region of interest (ROI) around the depth of the capillary was selected in the filtered RF data. The Fast Fourier Transform (FFT) was calculated for the RF data inside the selected ROI. Finally, the obtained frequency spectrum was compensated for the transmit-receive characteristics of the transducer.

The fundamental and harmonic frequency spectra, obtained without applying SVD filtering, are shown in Figure 4.3d and g, respectively. In the fundamental frequency spectrum a peak is observed at the transmit frequency of the narrowband pulse (i.e. $2\,\mathrm{MHz}$). The FFT of the harmonic response shows a peak at both once and twice the transmit frequency. The amplitudes of the fundamental and harmonic peaks were determined and plotted on a dB scale as a function of the chosen singular value limit, as shown in Figure 4.3a and b. The amplitude of the fundamental response was taken as the peak amplitude at the transmit frequency in the fundamental frequency spectra, while the harmonic amplitude was obtained from the peak at twice the transmit frequency in the harmonic frequency spectra. As the level of SVD filtering increases, more background noise is removed causing the baseline of the frequency spectra to decrease. To compensate for this, a linear fit was applied to establish the noise ground level. Subsequently, the baseline values at the fundamental and harmonic frequencies were determined for each spectrum and subtracted from the corresponding fundamental and harmonic amplitudes. In Figure 4.3b, the second part of the harmonic response curve for the wire is depicted as a dashed line since the harmonic amplitude was barely distinguishable from the noise baseline.

Figure 4.3a and b show that the amplitude of both the fundamental and harmonic response decreases as the singular value limit increases. The fastest decrease is observed when moving from a singular value lower limit of 1 to 2, which corresponds to the removal of stationary background signal. After the removal of around 3 to 4 principal components, the decrease becomes approximately linear on the dB scale, implying an exponential decrease. The decrease in amplitude of the fundamental response is similar for the beads and the bubbles, whereas the fundamental response corresponding to the wire decreases more rapidly. It decreases down to a negligible amplitude of -70 dB at a lower limit of 4 singular values, as expected for a stationary scatterer. Similarly, the harmonic response decreases faster when using a wire as acoustic scatterer compared to using microbubbles or beads. The harmonic response of the beads and the microbubbles show a similar trend with a difference in amplitude of a few dB. A larger difference of about 12 dB is observed when comparing the curves for the 1.5 and $2\,\mathrm{MHz}$ narrowband pulse. The SVD filter seems to attenuate higher frequencies more rapidly than lower frequencies. This is also confirmed by the faster decrease in the harmonic signal compared to the fundamental signal of the wire. This difference could also partially be attributed to an imperfect

compensation for the transducer characteristics.

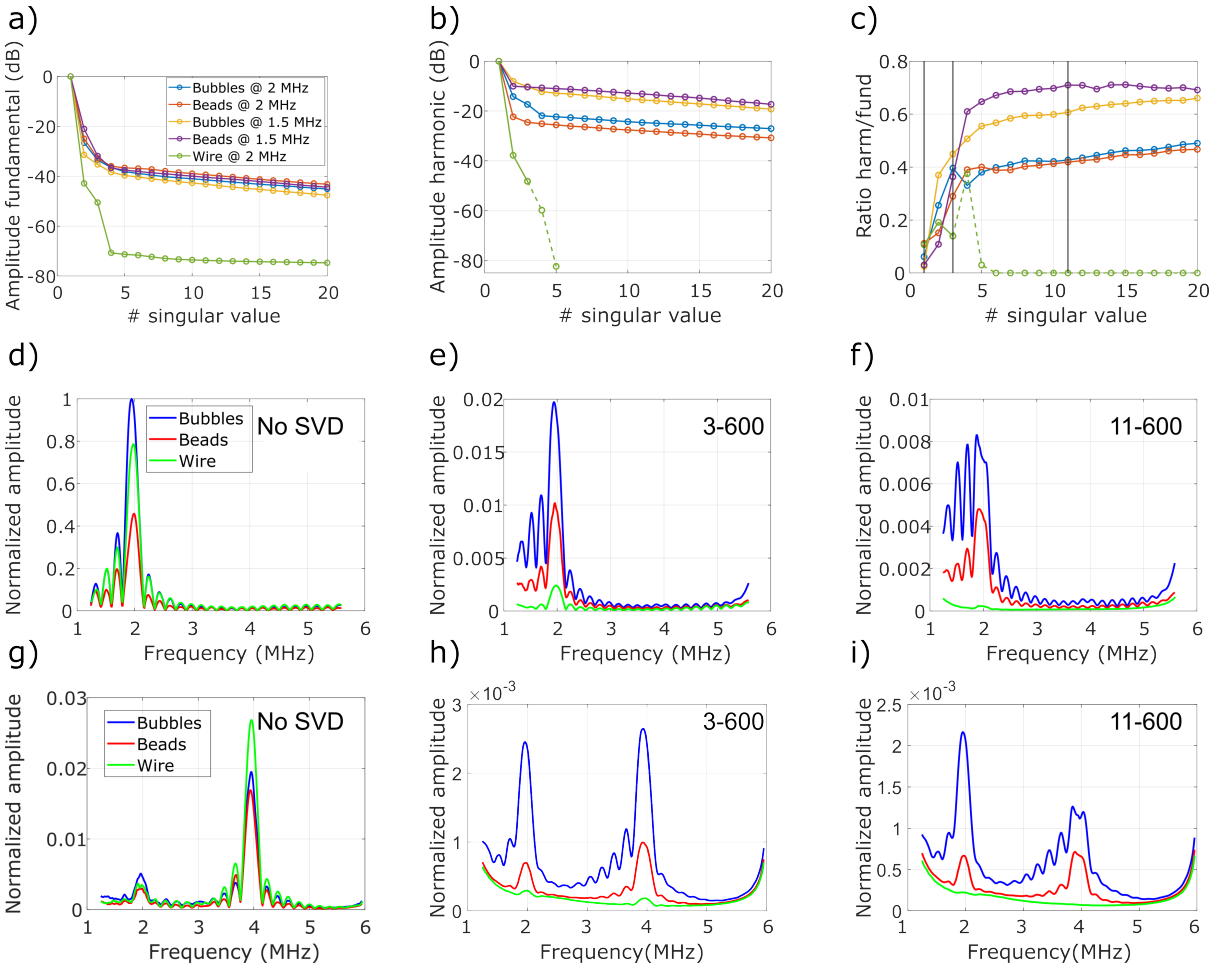

Figure 4.3: (a-b) Amplitude of peak at fundamental frequency in spectra (d-f) and harmonic frequency in spectra (g-i) versus the singular value lower limit. (c) Ratio of harmonic and fundamental amplitude versus the singular value lower limit. Curves are shown for a wire, beads and microbubbles driven by narrowband ultrasound waveforms at 1.5 and $2\,\mathrm{MHz}$. (d-f) Fundamental frequency response and (g-i) harmonic frequency response of beads, a wire and microbubbles on a narrowband $2\,\mathrm{MHz}$ ultrasound pulse for several levels of SVD filtering.

In addition to studying the absolute amplitudes of the fundamental and harmonic responses, it is relevant to analyze the ratio between the two. The ratio provides insight into the degree of non-linearity present in the ultrasound signal, which is essential for studying the nonlinear behaviour of the microbubbles. The ratio between the harmonic and fundamental amplitude as a function of the chosen singular value limit for the beads, wire and microbubbles is shown in Figure 4.3c for transmit frequencies of 1.5 and $2\,\mathrm{MHz}$. Figure 4.3c shows that the chosen singular value limit significantly influences the ratio between the measured harmonic and fundamental response. Up to a singular value of 3 or 4 the ratio rapidly increases. For singular values above 5 the ratio of the beads and microbubbles becomes approximately constant although with a slight increase. At this same singular value limit, the ratio of the wire drops to zero implying that static signal is removed. The ratio

corresponding to the different transmit frequencies and types of moving acoustic scatterers show a similar shape. However, the ratio for the beads and the microbubbles show a difference on the order of 0.02 to 0.1. Furthermore, the ratio increases more by a factor of around 1.5 for a lower transmit frequency. This is in accordance with the faster decrease in the harmonic amplitude, as observed in Figure 4.3c.

As the fundamental and harmonic amplitudes show a stable exponential decrease after a certain singular value limit and the ratio appears to converge, it seems possible to perform a quantitative analysis of the frequency content after SVD filtering. However, we still need to investigate whether there exists an accurate relation between the obtained amplitudes and the acoustic response generated by the microbubbles and the beads. A positive indication is that the remaining amplitudes, after removal of around 4 principal components, seem to be associated to the moving scatterers since the static signal of the wire has already been removed at this stage.

To see the effect of the SVD filtering on the shape of the frequency spectra, the frequency spectra were plotted for three levels of SVD filtering in Figure 4.3d to i. The graphs show the FFT after SVD filtering with lower limits of 1 (i.e. no SVD filtering), 3 and 11. These lower limits are depicted by the vertical lines in Figure 4.3c. The lower limit of 3 is in the regime where the ratio still increases, while the ratio is approximately constant for a lower limit of 11. Figure 4.3d to f correspond to the fundamental RF spectra and Figure 4.3g to i to the harmonic spectra. The amplitudes were normalized with respect to the maximum amplitude of the microbubble signal without applying SVD filtering. From Figure 4.3d to f, we observe that the peak is distorted: it becomes flatter and less distinguishable from the surrounding signal, when increasing the lower limit. The FFTs of the harmonic response (Figure 4.3g to i) show a peak at the fundamental frequency, which has not been cancelled out by applying pulse inversion. This peak becomes larger with respect to the harmonic response in the spectrum as more singular values are removed.

Beside the influence of SVD filtering on the spectral content of the data, we also studied the influence on the reconstructed ultrasound images. The fundamental and harmonic RF data was filtered and reconstructed with 3 and 11 as lower limits for the SVD filtering. The fundamental and harmonic reconstructed images are shown in Figure 4.4, together with the images reconstructed for unfiltered data. Figure 4.4a to f show the phantom with the wire, while Figure 4.4g to l show the capillary phantom perfused with microbubbles. The reconstructed images of the wire show that SVD filtering reduces the average fundamental signal from above -6 dB to below -55 dB after removing 10 singular values, while reducing the harmonic signal from approximately -36 dB to below -57 dB. Around the location of the wire, SVD filtering reduces the average fundamental signal intensity from 16 to -52 dB. The harmonic signal from the wire decreases from -17 dB down to -56 dB. The SVD filtering can thus filter out signal from static tissue, as was already observed earlier.

The reconstructed images of the capillary phantom (Figure 4.4g to l) show that signal emanating from the capillary can already be distinguished from the surrounding tissue without applying SVD filtering. The SVD filtering does not significantly reduce the signal originating from the water and PVCP. The fundamental signal's average intensity in the water and PVCP is approximately -55 dB and -40 dB, respectively, both before and after the application of SVD filtering. Similarly, the difference between the harmonic signal's average intensity before and after SVD filtering is less than 2 dB. The signal is approximately -60 dB in the water and -55 dB in the PVCP. The limited reduction in the water signal can be attributed to moving impurities in the water. Vibrations induced by pumping fluid through the

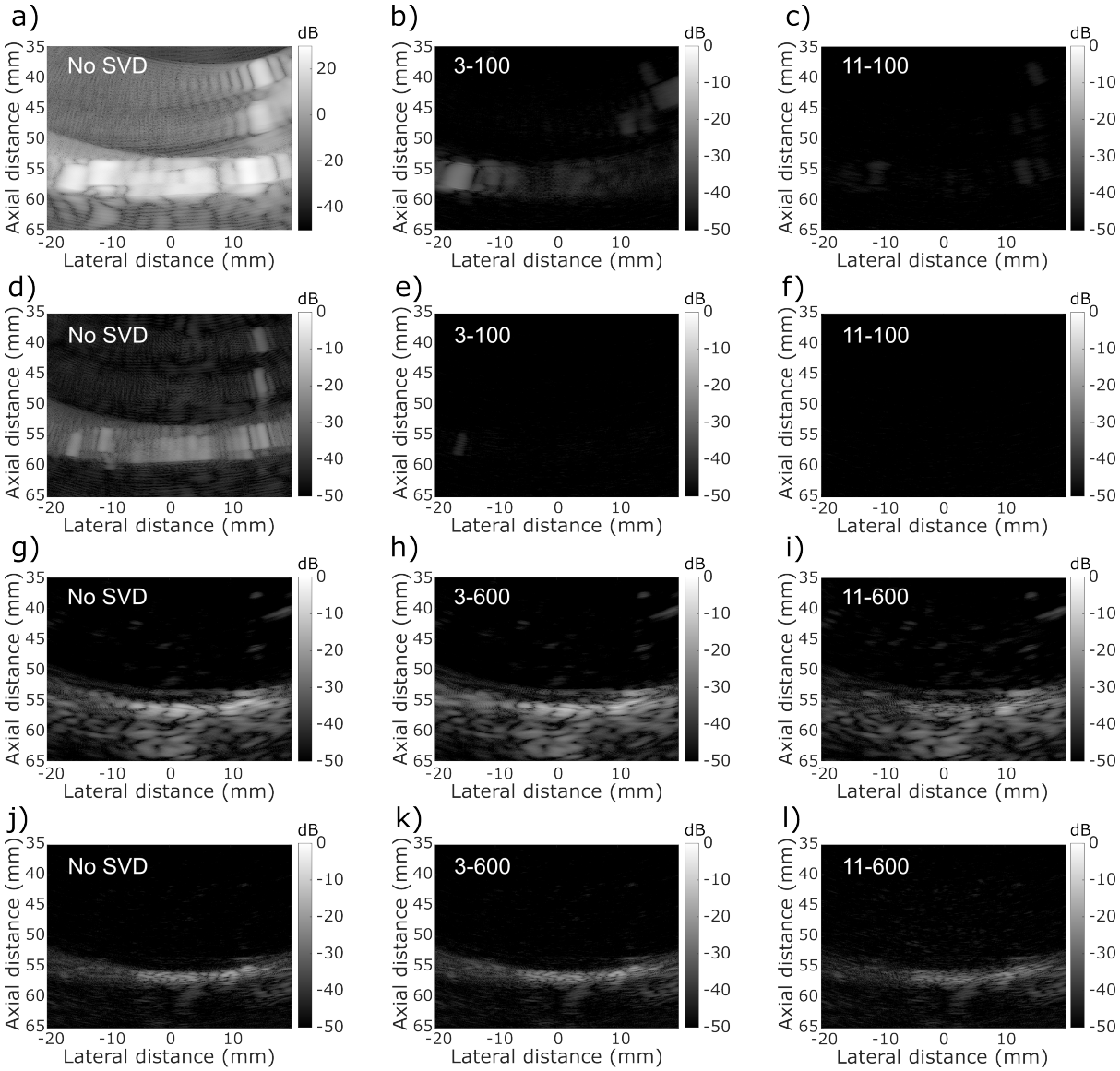

Figure 4.4: (a-c) Reconstructed images of fundamental RF data of the wire phantom for several levels of SVD filtering. (d-f) Reconstructed images of harmonic RF data of the wire phantom for several levels of SVD filtering. (g-i) Reconstructed images of fundamental RF data for several levels of SVD filtering with microbubbles present in the capillary. (j-l) Reconstructed images of harmonic RF data for several levels of SVD filtering with microbubbles present in the capillary.

capillary might explain the limited removal of signal in the PVCP. These movement and vibrations result in reduced spatio-temporal coherence inside the water and the PVCP causing the SVD filter to not filter out the signal. When increasing the lower limit, mainly the signal coming from the region of the capillary is removed. Around the capillary, the fundamental signal is reduced from -26 dB to -33 dB, while the harmonic signal reduces by around 3 dB from -37 dB to -40 dB due to SVD filtering. From these observations we can conclude that SVD filtering does not significantly enhance the signal-to-background ratio of the signal from the beads or microbubbles with respect to the surrounding tissue. Since more Fourier filtering was applied before reconstructing the microbubble

images, no direct comparison can be made with the images of the wire.

4.4 Simulation model

4.4.1 Time step convergence study

To determine which time step size to use for the simulations, we studied the convergence of the time step size. We ran the simulation with an ultrasound driving frequency of $0.3\,\mathrm{MHz}$. Each run, the time step size was halved with respect to the former step size. The evolution of the bubble radius over time was extracted from the simulations. The bubble radius versus time is plotted for time step sizes of 1, 2, 4 and $8\,\mathrm{ns}$ in Figure 4.5a. The relative error between the bubble radius at each time step size with respect to the radius at the smallest step size was calculated using the L2 norm. Subsequently, the error was normalized to obtain the Root Mean Square Error (RMSE):

$$\text{RMSE } R(\Delta t) = \sqrt{\frac{1}{n}\sum_{i=1}^{n} |R_{\Delta t} - R_{\Delta t_{ref}}|^2}, \tag{4.1}$$

where $R_{\Delta t}$ is the radius for a time step size of Δt and Δt_{ref} corresponds to the smallest time step size of $1\,\mathrm{ns}$. n is the number of data points of the simulation. Figure 4.5b shows the errors obtained for each step size on a logarithmic scale.

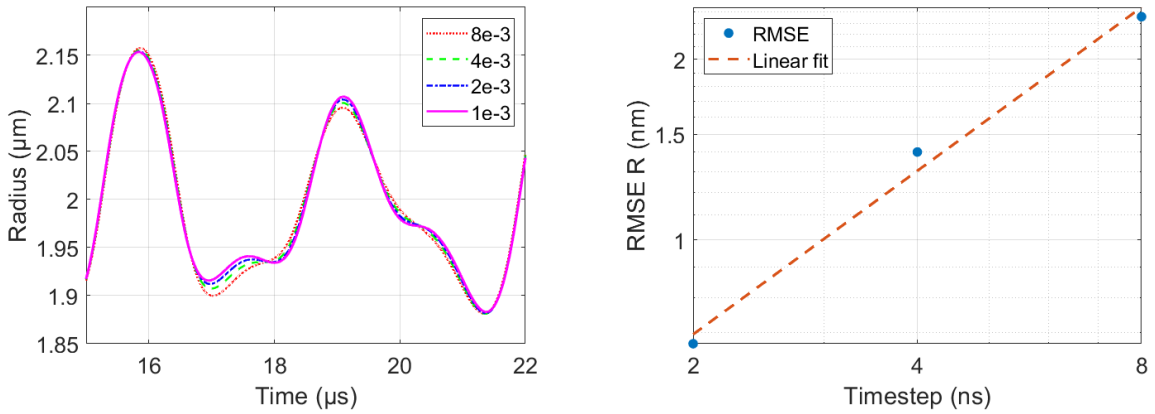

(a) (b)

Figure 4.5: (a) Bubble radius over time for several time step sizes. The legend shows the time step size in µs. (b) Root Mean Square Error (RMSE) of the bubble radius with respect to $\Delta t = 1\,\mathrm{ns}$ as a function of time step size, plotted on a logarithmic scale. The linear fit is shown by the dashed line and has a slope of 0.9.

Figure 4.5b shows that the error decreases when decreasing the time step size. A linear fit of the errors gave a slope of approximately 0.9, which suggests a linear convergence of the simulation. However, it is important to note that this fitting is based on no more than three data points. For a step size of 2 ns the error reduces to $0.7\,\mathrm{nm}$, which is around 0.04% of the initial bubble radius. As this error was considered sufficiently small, a time step size of $2\,\mathrm{ns}$ was chosen for the subsequent simulations.

4.4.2 Bubble oscillation and wall deformation

Figure 4.6a and b show the bubble oscillations and the left wall displacement, observed in the numerical simulations. The frames were taken at time intervals of 400 ns. From the initial to the final frame, the bubble shows expansion and the wall moves towards the left, indicating displacement away from the bubble.

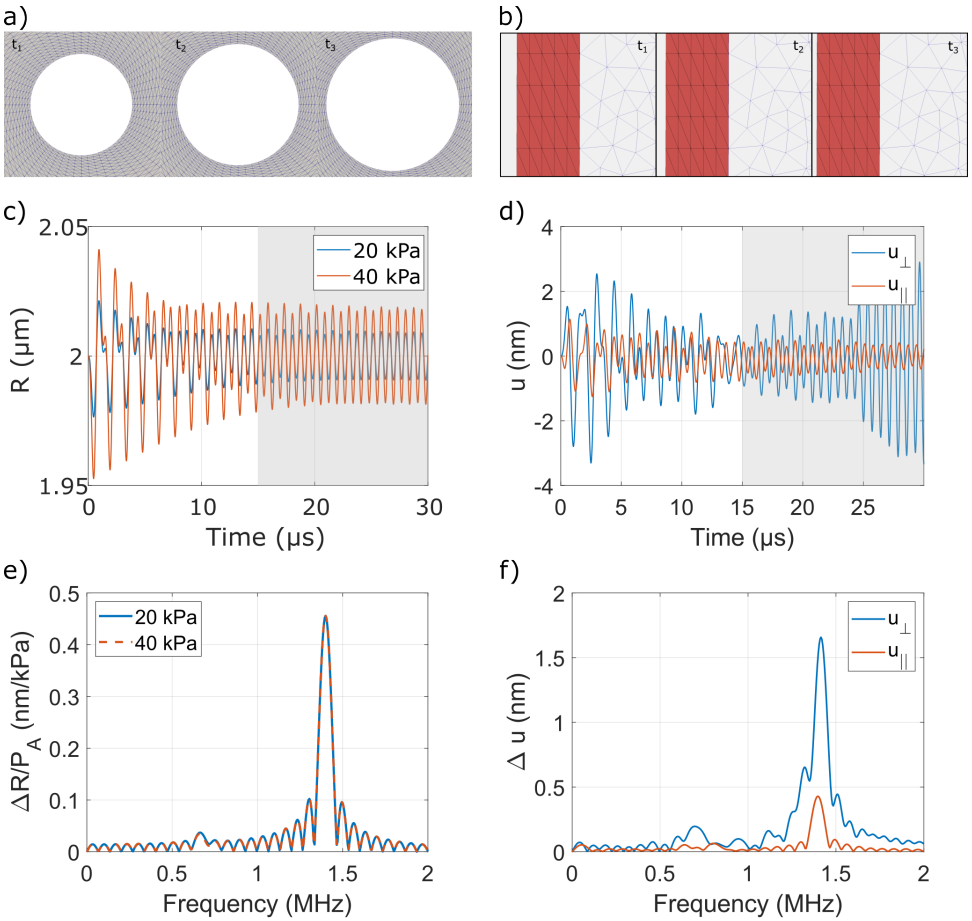

Figure 4.6: (a) Frames of numerical simulation taken at time intervals of 400 ns showing bubble oscillation and (b) wall movement. (c) Bubble radius over time for an ultrasound driving frequency of $1.4\,\mathrm{MHz}$ and driving pressures of 20 and $40\,\mathrm{kPa}$. (d) Wall displacement orthogonal and parallel to the wall over time for an ultrasound driving frequency of $1.4\,\mathrm{MHz}$ and a driving pressures of $40\,\mathrm{kPa}$. (e-f) Fast Fourier transform of the curves shown in (c) and (d). In (e) the amplitude is divided by the acoustic pressure.

The evolution of the bubble radius over time was extracted from the simulation data and plotted for several ultrasound driving frequencies and pressures. Figure 4.6c shows the bubble radius over time curves for an ultrasound frequency of 1.4 MHz and pressures of 20 and $40\,\mathrm{kPa}$. Moreover, the displacement of the wall orthogonal and parallel to the wall surface was determined for an ultrasound frequency of 1.4 MHz and a pressure of $40\,\mathrm{kPa}$, as shown in Figure 4.6d. For these simulations, the shear modulus and bulk modulus of the walls were $250\,\mathrm{kPa}$ and $962\,\mathrm{MPa}$, respectively.

Subsequently, the Fast Fourier transform (FFT) of the oscillating radius and the wall displacement was

determined. Some transient behaviour can be observed in Figure 4.6c and d before the oscillations stabilize. Since the ultrasound wave is a continuous wave without an envelope, the ultrasound pressure experienced by the microbubble is not built up gradually causing this transient in the oscillations. To minimize the effect of the transient, the FFT was calculated based on the second half of the data, depicted by the shaded area. Figure 4.6e and f show the corresponding FFTs. The FFTs of the radial oscillations were divided by the acoustic driving pressure.

Figure 4.6c shows that the oscillation amplitude is lower for a smaller pressure, according to expectations. As shown in Figure 4.6e, the frequency is found to be around $1.4\,\mathrm{MHz}$, which corresponds to the driving frequency. Moreover, the FFTs of the oscillations at different pressures overlap when compensated for the acoustic driving pressure. The smaller peak, shown in the FFT around $0.66\,\mathrm{MHz}$, is caused by the transient behaviour of the bubble oscillations. Figure 4.6d and f show that the wall displacement orthogonal to the surface is larger than parallel to the wall surface, as expected. Similar as for the bubble radius, the wall displacement oscillates at the driving frequency of the ultrasound, i.e. $1.4\,\mathrm{MHz}$.

The maximum amplitude of the bubble radius was determined for the stabilized (shaded) part of the bubble oscillations for each driving frequency. The maximum amplitude was plotted against the driving frequency for ultrasound pressures of 20 and $40\,\mathrm{kPa}$. The curves obtained are shown in Figure 4.7. Moreover, a simulation was run with a higher wall stiffness. To increase the wall stiffness, the shear modulus was increased from $250\,\mathrm{kPa}$ to $250\,\mathrm{MPa}$ and the bulk modulus was increased from $962\,\mathrm{MPa}$ to $962\,\mathrm{GPa}$. The curve for a higher wall stiffness is also shown in Figure 4.7.

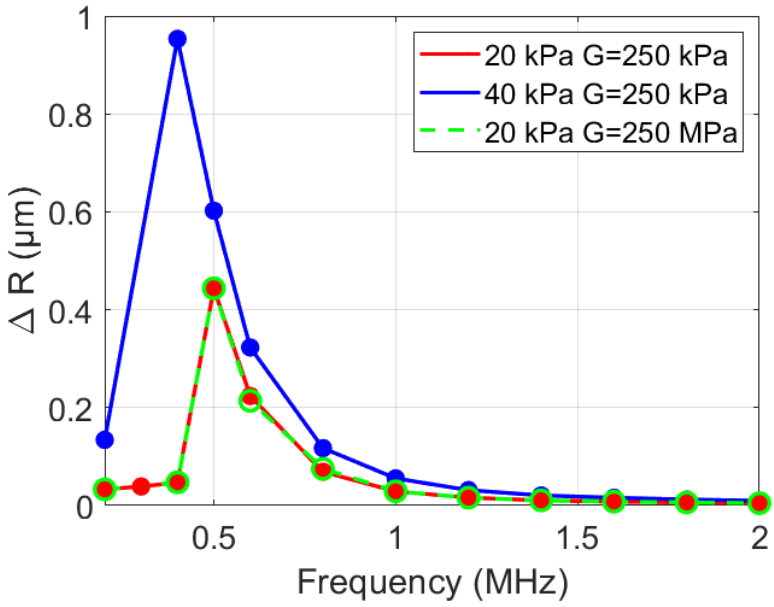

Figure 4.7: Maximum amplitude of the radial oscillations of the bubble as a function of ultrasound driving frequency for different ultrasound driving pressures and values for the wall stiffness.

The curves in Figure 4.7 show clear peaks at 0.4 and $0.5\,\mathrm{MHz}$ for 20 and $40\,\mathrm{kPa}$, respectively. These peaks are evidence of resonance behaviour as expected from theory. Moreover, we observe that the resonance frequency decreases with increasing driving pressure and the skewness typical for resonance

curves of microbubbles is observed [8,9]. The resonance curves for different values of the shear and bulk modulus overlap, implying that the stiffness of the wall does not effect the resonance behaviour of the bubble. This can be explained by the fact that the diameter of the capillary ($D = 100\,\mu\mathrm{m}$) is relatively large compared to the size of the microbubble ($R = 2\,\mu\mathrm{m}$), resulting in no effective confinement of the microbubble. Since the numerical simulation is in 2D, the obtained resonance frequencies cannot be compared to values found in literature. For comparison with theory, the Rayleigh-Plesset equation should be derived in cylindrical coordinates.

5 | Discussion and outlook

The experimental and simulation results are promising for measuring and modelling the confined microbubble response. However, some improvements are still required.

5.1 Setup and data acquisition

In this study, the optical setup primarily served as a visualization tool during experiments to check whether acoustic scatterers, i.e. glass beads or microbubbles, were flowing through the capillary. Few high speed images were captured, which does not exploit the functionality of the setup. In the upcoming research, the optical high speed imaging setup will be used to record the microbubble oscillations during ultrasound actuation. This optical data can then serve as validation for the acoustical measurements.

For the capillary phantom, we used liquid plastisol (PVCP) because of its acoustic properties being similar to water and its resilience enabling perfusion of the capillaries. However, we still need to properly characterize the material by measuring the attenuation coefficient, speed of sound and acoustic impedance. The current phantom contains a single capillary. Another option would be to create a network of multiple capillaries. This will enhance the signal received from scatterers inside the capillaries with respect to the background signal. Moreover, having multiple capillaries will facilitate easier perfusion of the capillaries since the fluid can flow in multiple directions. This also implies that an obstruction in one of the capillaries will not stop the entire flow. Easier perfusion is especially important when we start using even smaller capillaries with diameters down to $15\,\mu\mathrm{m}$. A disadvantage, however, of multiple capillaries is that the optical setup can only visualize a single capillary. Furthermore, due to the spread in location of the capillaries, the scatterers inside different capillaries will experience different ultrasound pressures.

In addition to the chirp and narrowband pulses, a 'broadband' imaging pulse of 1 cycle with a center frequency of $2\,\mathrm{MHz}$ was used in the experiments, as illustrated in Figure 3.4. The RF data acquired using this short pulse was used for reconstructing the ultrasound images because of its increased resolution with respect to longer waveforms. However, this measured RF data was not used for data analysis since the -6 dB bandwidth of the 'broadband' pulse was only 22% of the transducer bandwidth, i.e. a bandwidth of $1.6\,\mathrm{MHz}$ to $2.7\,\mathrm{MHz}$, as depicted in Figure 3.4. In future research, we plan to design a true broadband pulse covering the entire transducer bandwidth. One approach involves decreasing the duration of the pulse and thereby broadening the bandwidth. A shorter pulse duration can be implemented by reducing the number of cycles as input for the tri-state signal generator of the Verasonics system. Furthermore, we plan to design and optimize the tri-state pulser ourselves for direct input into the Verasonics system. The Verasonics tri-state signal generator yields ultrasound waveforms showing frequency fluctuations, as can be seen for the chirp in Figure 3.4. Designing and optimizing the tri-state enables us to improve, for example, the chirp waveform by creating a uniform output pressure at each frequency and ensuring a frequency output without fluctuations.

To be able to distinguish between the harmonic signal originating from the nonlinear microbubble response and the nonlinear propagation effects, the amount of nonlinear propagation should be reduced. Since the amount of nonlinear propagation increases quadratically with increasing ultrasound

pressure [49], an option is to use focused ultrasound transmission instead of plane waves. In that case, the ultrasound pressure at the location of the focus can be kept at the same pressure while reducing the ultrasound pressure in the surrounding tissue. This leads to less nonlinear propagation effects from propagating through the surrounding water and tissue. Moreover, the distance between the ultrasound transducer and capillary phantom can be reduced to reduce the travel distance of the ultrasound waves and thus the amount of nonlinear propagation.

5.2 Signal filtering

After removal of a particular number of singular values in the SVD filtering, a stable exponential decrease in both the fundamental and harmonic responses was observed, along with the convergence of the ratio to a specific value. This indicates potential for a quantitative analysis of the frequency content after SVD filtering. However, we still need to investigate whether a relationship exists between the values found after SVD filtering and the acoustic response generated by the microbubbles and the beads. Moreover, we would need to study the frequency dependence of SVD filtering, which impacts, a priori, the spatio-temporal coherence. We could study these using the numerical simulator PROTEUS, developed by a collaboration between the UT and TU Delft. PROTEUS is an ultrasound RF data simulator for microbubbles in the bloodstream. We could apply SVD filtering on RF data from this simulator and compare the obtained frequency spectrum with the frequency response of purely microbubbles, i.e. without background signal and applying SVD filtering.

In addition to SVD filtering, we have used a combination of frequency and spatial filtering techniques. For frequency filtering we have used Pulse Inversion (PI), which was shown to separate the fundamental and harmonic frequency components quite well. An alternative is to separate the fundamental and harmonic response using frequency filtering based on the wavelet transform. A wavelet transform filter filters the data based on the frequency components of the signal, similar to Fourier filtering. Whereas the Fourier transform decomposes signals into sine waves of specific frequencies, the wavelet transform decomposes signals into scaled and shifted versions of a short wave, i.e. a wavelet. Therefore, the wavelet transform yields not only frequency information but also information on the localization of the signal in time. [50] Hence, we could potentially use the wavelet transform to isolate the desired frequency, either the fundamental or the harmonic frequency response. Thereafter, we can use spatial filtering to separate the signal originating from the capillary and the signal emanating from the surrounding tissue. In this thesis, some spatial filtering was applied by selecting a region of interest (ROI) around the depth of the capillary in the RF data. However, this filtered RF data still contains echoes originating from scatterers located at the same depth as the capillary. We could improve the spatial filtering by filtering directly on the IQ data. The IQ data is obtained after beamforming the RF data, but before performing demodulation and log compression to get the reconstructed image. Therefore, the IQ data is a 2D representation of the data but still contains both the amplitude and the phase information of the received echoes. In the IQ data it is then possible to isolate the signal specifically originating from the location of the capillary.

5.3 Simulation

In the results of the numerical simulations, an oscillation of the microbubble and elastic walls was observed at the ultrasound driving frequency. The oscillation amplitude of the microbubble as a

function of driving frequency showed a skewed resonance curve with the resonance frequency depending on the ultrasound pressure. These findings are promising since they are in accordance with what is expected from literature. However, the numerical study still has limitations. First, the resonance frequency showed no dependence on the wall stiffness due to the diameter of the capillary being relatively large compared to the microbubble size. To increase the confinement of the microbubble, the diameter of the capillary in the simulation should be reduced. Second, the numerical simulation models the capillary walls as a hyperelastic solid. However, capillaries are viscoelastic. Therefore, we could improve the representation of the capillary wall behaviour by implementing an elasto-viscoplastic model like the one proposed by Saramito [51]. Moreover, the current implementation of the microbubble boundary movement does not account for nonspherical oscillations of the microbubble. The pressure boundary condition at the bubble wall is namely calculated using the average bubble radius. However, since we already determine the local radius of the bubble, it requires small alterations to change from a global pressure boundary condition to a local one, thereby allowing for nonspherical oscillations.

While running the simulations with a driving frequency around the resonance frequency, numerical instability was observed. Therefore, the actual amplitude of the resonance peak might differ from the amplitude shown in Figure 4.7. The numerical instabilities were caused by nonuniform deformations of the walls leading to mesh distortion. Using strong coupling instead of weak coupling to couple the fluid and solid structure could improve the stability, as discussed in chapter 2.

Finally, since the numerical simulation framework is two-dimensional, no quantitative comparison can be made with experimental findings. Although, the current simulation model is ready for a transition from 2D to 3D, the simulation has been in 2D up to now to save computational time. The next step for the numerical simulations is to transition from a two-dimensional to a three-dimensional geometry to allow for experimental validation of the numerical results.

The goal for the upcoming years is to improve on these limitations and expand the simulations and experiments to study the effect of tube diameter, vessel stiffness and the location of the microbubble in the capillary on the microbubble response.

6 | Conclusion

In this thesis, we have taken the first steps towards a model relating the microbubble response to vessel properties by focusing on three different aspects: experiments, signal filtering and numerical simulations. In the experimental part, we have built an experimental setup combining ultrasound imaging and high speed optical imaging. Moreover, we have created a capillary phantom, which could be perfused with acoustic scatterers. We have found liquid plastisol (PVCP) to be the most suitable tissue-mimicking material for the capillary phantom due to its acoustic properties being similar to water and its resilience enabling perfusion of the capillaries. The optical setup could visualize the scatterers moving through the capillary phantom. Using the acoustical setup, we have measured the acoustic response from coated microbubbles and hollow glass beads in the capillary phantoms using chirp and narrowband pulses.

When comparing the acoustic response of the microbubbles and the beads, both scatterers showed higher harmonics. This implies that the acoustic measurements lack the sensitivity needed to differentiate between higher harmonics generated by the nonlinear microbubble response and harmonic signal generated by, for example, nonlinear propagation. As we have not yet successfully isolated the nonlinear microbubble response from the effects of nonlinear propagation, we cannot draw definitive conclusions regarding the optimal waveform. Nevertheless, the broadband pulse and the chirp offer an advantage by transmitting all frequencies either simultaneously or within a very brief time span, thereby minimizing the effects from movement of the scatterers and fluctuations in microbubble or beads concentration. In contrast, narrowband pulses are influenced by movement and fluctuations, as they require sweeping over frequencies while adjusting the transducer voltage simultaneously to maintain a constant pressure output. Obtaining a constant pressure output, however, is unfeasible for the broadband pulse and complex for the chirp.

Pulse Inversion (PI) is capable of isolating the fundamental and harmonic responses. Furthermore, we have observed that SVD filtering effectively removed signal from stationary scatterers. No significant enhancement in the signal-to-background ratio of the capillary phantom images was observed due to movement of the phantom material. The analysis of the effect of SVD filtering on the spectra content of the data showed that a quantitative analysis of the frequency response is still possible after applying SVD filtering. As discussed in chapter 5, further research is needed to investigate the relation between the obtained amplitudes and the acoustic response generated by the microbubbles and the beads.

In addition to the experiments and data analysis, we have developed a 2D numerical simulation to study the dynamics of an ultrasound-driven microbubble confined between elastic walls. In the simulation, we have observed the microbubble oscillations and wall displacement to follow the oscillations of the ultrasound driving frequency. The microbubble oscillations showed a resonance behaviour. A decrease in resonance frequency with increasing ultrasound pressure was observed, which is in accordance with literature. However, no dependence on wall stiffness was observed due to the relatively large capillary diameter compared to the microbubble size. In order to experimentally validate the obtained resonance frequencies, the simulation needs to be transitioned from 2D to 3D.

Acknowledgements

First of all, I would like to thank my supervisors Guillaume and Michel for guiding me during this research, teaching me a lot and providing me with the opportunity to continue as a PhD student. I am also very thankful for the opportunity to travel to Sophia Antipolis to learn about numerical simulations. I would like to extend my gratitude to Elie and Anselmo, who made me feel very welcome there and taught me how to develop a numerical simulation with very little prior knowledge. Also thanks to all other colleagues at CEMEF for giving me a pleasant stay. Special thanks goes to Aurèle, who was always open to questions and was a great help in developing the simulation. I am looking forward to welcome you here in Enschede. I would also like to thank Ali and Nathan. I could always count on your help. Furthermore, I would like to thank the technicians: Gert-Wim, Martin and Thomas for helping me build the experimental setup. Great thanks as well to my other colleagues for the nice discussions and, of course, the tea breaks. I look forward to working with all of you in the upcoming four years. I would also like to thank Nienke for participating in my examination committee. Last but not least, I want to thank my family and friends for always supporting me.

Bibliography

[1] Jeremy Jones and Matt Morgan. Ultrasound (introduction). In *Radiopaedia.Org*. Radiopaedia.org, 2014.

[2] Thomas L. Szabo. Introduction. In *Diagnostic Ultrasound Imaging: Inside Out*, pages 1–37. Elsevier, 2014.

[3] Sania Ajmal. Contrast-Enhanced Ultrasonography: Review and Applications. 13(9):e18243, 2021.

[4] Arend F. L. Schinkel, Mathias Kaspar, and Daniel Staub. Contrast-enhanced ultrasound: Clinical applications in patients with atherosclerosis. 32(1):35–48, 2016.

[5] Hossein Yusefi and Brandon Helfield. Ultrasound Contrast Imaging: Fundamentals and Emerging Technology. 10:791145, 2022.

[6] Michel Versluis, Eleanor Stride, Guillaume Lajoinie, Benjamin Dollet, and Tim Segers. Ultrasound Contrast Agent Modeling: A Review. 46(9):2117–2144, 2020.

[7] Thomas L. Szabo. Ultrasound Contrast Agents. In *Diagnostic Ultrasound Imaging: Inside Out*, pages 605–651. Elsevier, 2014.

[8] Sander M. Van Der Meer, Benjamin Dollet, Marco M. Voormolen, Chien T. Chin, Ayache Bouakaz, Nico De Jong, Michel Versluis, and Detlef Lohse. Microbubble spectroscopy of ultrasound contrast agents. 121(1):648–656, 2007.

[9] Tim Segers, Nico De Jong, and Michel Versluis. Uniform scattering and attenuation of acoustically sorted ultrasound contrast agents: Modeling and experiments. 140(4):2506–2517, 2016.

[10] Shengping Qin, Charles F Caskey, and Katherine W Ferrara. Ultrasound contrast microbubbles in imaging and therapy: Physical principles and engineering. 54(6):R27–R57, 2009.

[11] Shengping Qin and Katherine W. Ferrara. The Natural Frequency of Nonlinear Oscillation of Ultrasound Contrast Agents in Microvessels. 33(7):1140–1148, 2007.

[12] H. N. Oguz and A. Prosperetti. The natural frequency of oscillation of gas bubbles in tubes. 103(6):3301–3308, 1998.

[13] Sergey Martynov, Eleanor Stride, and Nader Saffari. The natural frequencies of microbubble oscillation in elastic vessels. 126(6):2963–2972, 2009.

[14] Dietmar W. Siemann. The unique characteristics of tumor vasculature and preclinical evidence for its selective disruption by Tumor-Vascular Disrupting Agents. 37(1):63–74, 2011.

[15] J A Nagy, S-H Chang, A M Dvorak, and H F Dvorak. Why are tumour blood vessels abnormal and why is it important to know? 100(6):865–869, 2009.

[16] Charles F. Caskey, Dustin E. Kruse, Paul A. Dayton, Tyler K. Kitano, and Katherine W. Ferrara. Microbubble oscillation in tubes with diameters of 12, 25, and 195 microns. 88(3):033902, 2006.

[17] David H. Thomas, Vassilis Sboros, Marcia Emmer, Hendrik Vos, and Nico De Jong. Microbubble oscillations in capillary tubes. 60(1):105–114, 2013.

[18] Hairong Zheng, Paul A. Dayton, Charles Caskey, Shukui Zhao, Shengping Qin, and Katherine W. Ferrara. Ultrasound-Driven Microbubble Oscillation and Translation Within Small Phantom Vessels. 33(12):1978–1987, 2007.

[19] Philippe Marmottant, Sander Van Der Meer, Marcia Emmer, Michel Versluis, Nico De Jong, Sascha Hilgenfeldt, and Detlef Lohse. A model for large amplitude oscillations of coated bubbles accounting for buckling and rupture. 118(6):3499–3505, 2005.

[20] Michalakis A. Averkiou, Matthew F. Bruce, Jeffry E. Powers, Paul S. Sheeran, and Peter N. Burns. Imaging Methods for Ultrasound Contrast Agents. 46(3):498–517, 2020.

[21] Thomas L. Szabo. Nonlinear Acoustics and Imaging. In *Diagnostic Ultrasound Imaging: Inside Out*, pages 501–563. Elsevier, 2014.

[22] Che-Chou Shen, Yi-Hong Chou, and Pai-Chi Li. Pulse Inversion Techniques in Ultrasonic Nonlinear Imaging. 13(1):3–17, 2005.

[23] Hayato Ikeda, Ryo Nagaoka, Maxime Lafond, Shin Yoshizawa, Ryosuke Iwasaki, Moe Maeda, Shin-ichiro Umemura, and Yoshifumi Saijo. Singular value decomposition of received ultrasound signal to separate tissue, blood flow, and cavitation signals. 57:07LF04, 2018.

[24] Charlie Demene, Thomas Deffieux, Mathieu Pernot, Bruno-Felix Osmanski, Valerie Biran, Jean-Luc Gennisson, Lim-Anna Sieu, Antoine Bergel, Stephanie Franqui, Jean-Michel Correas, Ivan Cohen, Olivier Baud, and Mickael Tanter. Spatiotemporal Clutter Filtering of Ultrafast Ultrasound Data Highly Increases Doppler and fUltrasound Sensitivity. 34(11):2271–2285, 2015.

[25] Jerome Baranger, Bastien Arnal, Fabienne Perren, Olivier Baud, Mickael Tanter, and Charlie Demene. Adaptive Spatiotemporal SVD Clutter Filtering for Ultrafast Doppler Imaging Using Similarity of Spatial Singular Vectors. 37(7):1574–1586, 2018.

[26] Vincent Perrot, Maxime Polichetti, François Varray, and Damien Garcia. So you think you can DAS? A viewpoint on delay-and-sum beamforming. 111:106309, 2021.

[27] Verasonics. Vantage Sequence Programming Manual, 2019.

[28] *Diagnostic Ultrasound Imaging: Inside Out*. Elsevier, 2014.

[29] Peiran Chen, Andreas M.A.O. Pollet, Anastasiia Panfilova, Meiyi Zhou, Simona Turco, Jaap M.J. Den Toonder, and Massimo Mischi. Acoustic characterization of tissue-mimicking materials for ultrasound perfusion imaging research. 48(1):124–142, 2022.

[30] Adrian F Prokop, Shahram Vaezy, Misty L Noble, Peter J Kaczkowski, Roy W Martin, and Lawrence A Crum. Polyacrylamide gel as an acoustic coupling medium for focused ultrasound therapy. 29(9):1351–1358, 2003.

[31] M Fonseca, B Zeqiri, P C Beard, and B T Cox. Characterisation of a phantom for multiwavelength quantitative photoacoustic imaging. 61(13):4950–4973, 2016.

[32] Guangyao Xu, Zhengyang Ni, Xizhou Chen, Juan Tu, Xiasheng Guo, Henrik Bruus, and Dong Zhang. Acoustic Characterization of Polydimethylsiloxane for Microscale Acoustofluidics. 13(5):054069, 2020.

[33] Jean K. Tsou, Jie Liu, Abdul I. Barakat, and Michael F. Insana. Role of Ultrasonic Shear Rate Estimation Errors in Assessing Inflammatory Response and Vascular Risk. 34(6):963–972, 2008.

[34] Maura Dantuma, Rianne Van Dommelen, and Srirang Manohar. Semi-anthropomorphic photoacoustic breast phantom. 10(11):5921, 2019.

[35] Gloria M Spirou, Alexander A Oraevsky, I Alex Vitkin, and William M Whelan. Optical and acoustic properties at 1064 nm of polyvinyl chloride-plastisol for use as a tissue phantom in biomedical optoacoustics. 50(14):N141–N153, 2005.

[36] Aurèle Goetz, Pablo Rico, Yves Chau, Jacques Sedat, Aurélien Larcher, and Elie Hachem. Proposal for numerical benchmarking of fluid-structure interaction in cerebral aneurysms. 2023.

[37] Pijush K. Kundu, Ira M. Cohen, David R. Dowling, and Grétar Tryggvason. *Fluid Mechanics*. Elsevier/AP, sixth edition edition, 2016.

[38] Jean Donea, Antonio Huerta, J.-Ph. Ponthot, and A. Rodríguez-Ferran. Arbitrary Lagrangian–Eulerian Methods. In *Encyclopedia of Computational Mechanics*. John Wiley, 2004.

[39] P. B. Ryzhakov, J. Marti, and N. Dialami. A Unified Arbitrary Lagrangian–Eulerian Model for Fluid–Structure Interaction Problems Involving Flows in Flexible Channels. 90(3):85, 2022.

[40] Charbel Habchi, Serge Russeil, Daniel Bougeard, Jean-Luc Harion, Thierry Lemenand, Akram Ghanem, Dominique Della Valle, and Hassan Peerhossaini. Partitioned solver for strongly coupled fluid–structure interaction. 71:306–319, 2013.

[41] E. Hachem, B. Rivaux, T. Kloczko, H. Digonnet, and T. Coupez. Stabilized finite element method for incompressible flows with high Reynolds number. 229(23):8643–8665, 2010.

[42] R. Nemer, A. Larcher, T. Coupez, and E. Hachem. Stabilized finite element method for incompressible solid dynamics using an updated Lagrangian formulation. 384:113923, 2021.

[43] Aurèle Goetz. PhD thesis. Unpublished.

[44] P. Causin, J.F. Gerbeau, and F. Nobile. Added-mass effect in the design of partitioned algorithms for fluid–structure problems. 194(42-44):4506–4527, 2005.

[45] Tim Segers, Emmanuel Gaud, Michel Versluis, and Peter Frinking. High-precision acoustic measurements of the nonlinear dilatational elasticity of phospholipid coated monodisperse microbubbles. 14(47):9550–9561, 2018.

[46] Benjamin Van Elburg, Gonzalo Collado-Lara, Gert-Wim Bruggert, Tim Segers, Michel Versluis, and Guillaume Lajoinie. Feedback-controlled microbubble generator producing one million monodisperse bubbles per second. 92(3):035110, 2021.

[47] Tim Segers, Emmanuel Gaud, Gilles Casqueiro, Anne Lassus, Michel Versluis, and Peter Frinking. Foam-free monodisperse lipid-coated ultrasound contrast agent synthesis by flow-focusing through multi-gas-component microbubble stabilization. 116(17):173701, 2020.

[48] Mike Vega. GE Transducers for Vantage Systems.

[49] Martin D. Verweij, Libertario Demi, and Koen W. A. Van Dongen. Computation of nonlinear ultrasound fields using a linearized contrast source method. 134(2):1442–1453, 2013.

[50] Wavelet Transforms in MATLAB.

[51] Pierre Saramito. A new elastoviscoplastic model based on the Herschel–Bulkley viscoplastic model. 158(1-3):154–161, 2009.

A | Appendix

A.1 Calibration of the C1-6D probe

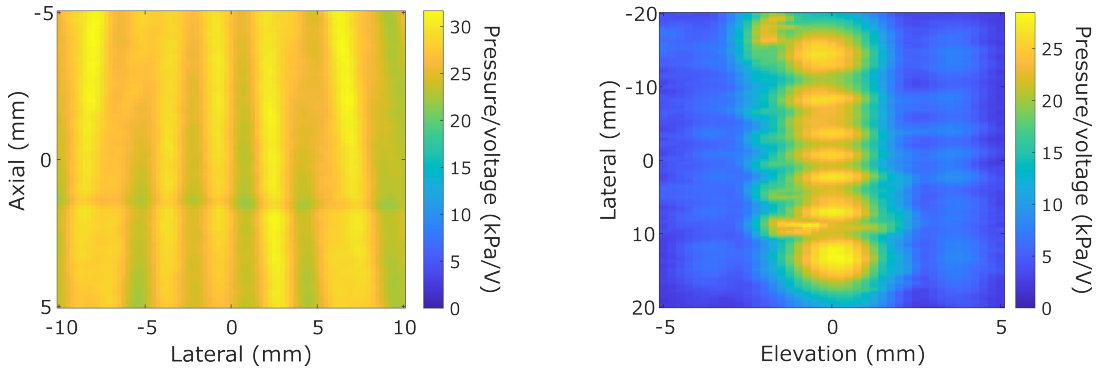

Figure A.1: (Left) The XY pressure field measured by the hydrophone for a narrowband pulse of $3\,\mathrm{MHz}$ transmitted by the C1-6D probe. (Right) The YZ pressure field measured by the hydrophone for a narrowband pulse of $3\,\mathrm{MHz}$ transmitted by the C1-6D probe.

A.2 Simulation parameters

Table A.1: Parameters used in the numerical simulation.

Physical constant	Symbol	Value	Unit
Fluid dynamic viscosity	μ_f	1e-3	Pas
Fluid density	ρ_f	1e3	kgm^{-3}
Solid density	ρ_s	0.98e3	kgm^{-3}
Atmospheric pressure	P_0	1e5	Pa
Polytropic exponent	κ	1.07	
Shell viscosity	κ_s	1e-8	kgs^{-1}
Shell elasticity	χ	0.5	kgs^{-2}
Speed of sound	c_l	1.5e3	ms^{-1}
Initial surface tension	σ_0	2e-2	kgs^{-2}
Surface tension water	σ_{water}	7.2e-2	kgs^{-2}
Shear modulus	G	2.5e5	Pa
Inverse bulk modulus	$\frac{1}{K}$	1.04e-9	Pa^{-1}

A.3 Acoustic response to narrowband pulse of 1.5 MHz

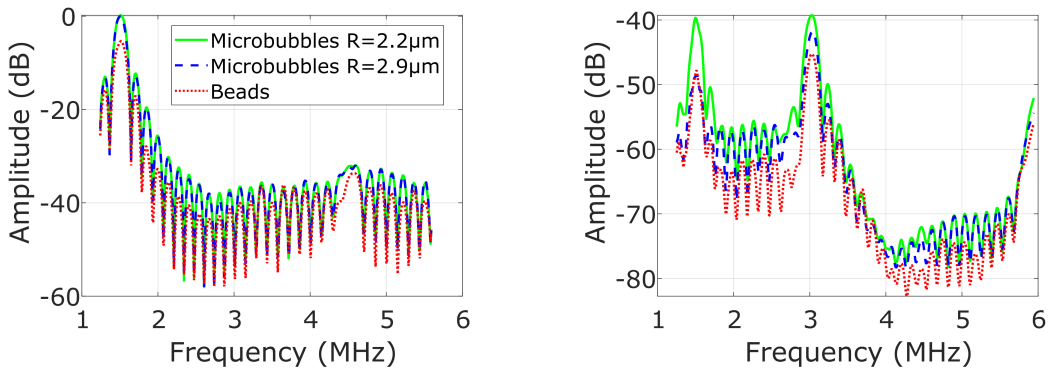

Figure A.2: (Left) Frequency spectra showing the fundamental response of microbubbles and beads to a narrowband pulse with a transmit frequency of $1.5\,\mathrm{MHz}$. (Right) Frequency spectra showing the harmonic response of microbubbles and beads to a narrowband pulse with a transmit frequency of $1.5\,\mathrm{MHz}$.